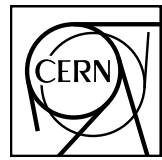


# EUROPEAN ORGANIZATION FOR NUCLEAR RESEARCH



May 22, 2017

## D-hadron correlations in p-Pb collisions at $\sqrt{s_{NN}} = 5.02 \text{ TeV}$

F. Colamaria, S. Kumar, M. Mazzilli

### Abstract

In this note, we present the analysis of azimuthal correlations of D mesons and primary charged particles performed in the ALICE central barrel in p-Pb collisions at  $\sqrt{s_{NN}} = 5.02 \text{ TeV}$ , from 2016 data taking, in an extended  $p_T$  range and with additional observables with respect to p-Pb 2013 data analysis. After a description of the analysis strategy, corrections and systematic uncertainties, the results obtained for prompt  $D^0$ ,  $D^{*+}$  and  $D^+$  mesons in different ranges of transverse momentum of the D meson and of the associated particles are presented and compared to Monte Carlo models and, for the common  $p_T$  ranges and observables, to 2013 p-Pb analysis.



**1 Contents**

<b>2 1 Introduction and Motivation</b>	<b>2</b>
<b>3 2 Data/Monte Carlo samples and event selection</b>	<b>3</b>
<b>4 3 Analysis strategy</b>	<b>6</b>
5     3.1 Mass plots and cut optimization . . . . .	9
6     3.2 Code used for the analysis . . . . .	13
7     3.3 Further details on corrections . . . . .	14
8         3.3.1 Event Mixing . . . . .	14
9         3.3.2 Tracking and D-meson trigger efficiency . . . . .	17
10         3.3.3 Beauty feed-down . . . . .	21
11         3.3.4 Beauty feed-down . . . . .	25
<b>12 4 Systematic uncertainties and checks of analysis consistency</b>	<b>29</b>
<b>13 5 Results</b>	<b>30</b>
14     5.1 Comparing the three D meson correlation distributions . . . . .	30
15     5.2 Average of $D^0$ , $D^+$ and $D^{*+}$ results . . . . .	36
16     5.3 Fit observable $p_T$ trends and uncertainties . . . . .	43
17         5.3.1 Results for near-side yield and width, away-side yield and width, and baseline . .	44
18     5.4 Planned results for SQM approvals . . . . .	58
<b>19 6 Bibliography</b>	<b>59</b>

20 **1 Introduction and Motivation**

21 The study of the azimuthal correlations of heavy-flavour particles and charged particles at the LHC  
 22 energies provides a way to characterize charm production and fragmentation processes in pp collisions  
 23 as well as a way to probe our understanding of QCD in the perturbative regime, accessible in a large  
 24 kinematic range given the large mass of heavy quarks. Flavour conservation in QCD implies that charm  
 25 quarks are always produced as pairs of quarks and anti-quarks. The azimuthal correlations obtained  
 26 using a meson carrying a heavy quark as trigger particle with the other charged particles in the same  
 27 event give the possibility to study the underlying charm production mechanism in detail. In particular,  
 28 prompt charm quark-antiquark pair production is back to back in azimuth at first order in leading-order  
 29 perturbative-QCD (pQCD). Heavy quarks produced from the splitting of a massless gluon can be rather  
 30 collimated and may generate sprays of hadrons at small  $\Delta\phi$ . Finally, for hard-scattering topologies  
 31 classified as “flavour-excitation”, a charm quark undergoes a hard interaction from an initial splitting  
 32 ( $g \rightarrow c\bar{c}$ ), leading to a big separation in rapidity of the hadrons originating from the antiquark (quark)  
 33 with respect to the trigger D meson and contribute to a rather flat term to the  $\Delta\phi$ -correlation distribution.

34 Heavy-flavour correlation studies in more complex collision systems, like Pb-Pb, play a crucial role in  
 35 studying the modification of the fragmentation of charmed jets due to in-medium (or cold nuclear matter,  
 36 in case of p-Pb collisions) effects, in a similar way as it was done for di-hadron correlation studies in  
 37 heavy-ion collisions (see for example). Furthermore, the recent observation of long range correlations in  
 38 p-Pb for light flavour hadrons and for heavy-flavour decay electrons points to possible collective effects  
 39 or effects originating from gluon saturation in the initial state. More information could be extracted by  
 40 the eventual observation of the same effect with D mesons.

41

42 In the following, we describe the analysis strategy for the p-Pb 2016 data sample in all its steps, and we  
 43 describe the list of corrections and the estimation of the systematic uncertainties we performed. We then  
 44 present the results of  $\Delta\phi$  correlations, and quantitative observable extracted to fits to those distributions,  
 45 obtained for prompt  $D^0$ ,  $D^+$  and  $D^{*+}$  in different ranges of transverse momentum for the D-meson  
 46 (trigger particle) and the associated particles.

47 **2 Data/Monte Carlo samples and event selection**

48 The data samples used for the analyses were the FAST and CENT\_woSDD samples from periods LHC16q  
 49 and LHC16t (AOD samples). The reason for this choice is explained later on, in this section. It was ver-  
 50 ified, by looking at D-meson and track  $\eta$  and  $\phi$  distributions, and at the mixed-event correlation distri-  
 51 butions for each subsamples, that no visible differences arose for the four periods, hence it was possible  
 52 to perform the analysis directly on the merged samples without any bias.

53 The Monte Carlo productions adopted for this study were:

- 54 1. LHC17d2a\_fast\_new, a HIJING production with enrichment, for each event, of c or b quarks and  
 55 their decay chains, performed by PYTHIA6 with Perugia2011 tune, and with forced hadronic  
 56 decays of the charmed hadrons. This production was used for D-meson efficiency evaluation,  
 57 purity estimation and Monte Carlo closure test.
- 58 2. LHC17a2b\_cent\_woSDD and LHC17a2b\_fast, minimum-bias samples produced with DPMJET  
 59 generator, used for the evaluation of the tracking efficiencies.

60 Table 1 shows the list of runs used for the analysis, for each of the data taking periods, and of the Monte  
 61 Carlo productions used to evaluate the corrections:

62 The trigger mask request for the event selection is kINT7. Only events with a reconstructed primary  
 63 vertex within 10 cm from the centre of the detector along the beam line are considered for both pp  
 64 and p-Pb collisions. This choice maximises the detector coverage of the selected events, considering  
 65 the longitudinal size of the interaction region, and the detector pseudorapidity acceptances. For p-Pb  
 66 collisions, the center-of-mass reference frame of the nucleon-nucleon collision is shifted in rapidity by  
 67  $y_{NN} = 0.465$  in the proton direction with respect to the laboratory frame, due to the different per-nucleon  
 68 energies of the proton and the lead beams. Beam-gas events are removed by offline selections based  
 69 on the timing information provided by the V0 and the Zero Degree Calorimeters, and the correlation  
 70 between the number of hits and track segments in the SPD detector. This is automatically performed in  
 71 the Physic Selection, a positive outcome of which is required during our event selection. The minimum-  
 72 bias trigger efficiency is 100% for events with D mesons with  $p_T > 1$  GeV/c. For the analyzed data  
 73 samples, the probability of pile-up from collisions in the same bunch crossing is below 2% per triggered  
 74 event (in most of the runs, well below 1%). Events in which more than one primary interaction vertex  
 75 is reconstructed with the SPD detector (with minimum of 5 contributors, and a z distance greater than  
 76 0.8 cm) are rejected, which effectively removes the impact of in-bunch pile-up events on the analysis.  
 77 Out-of-bunch tracks are effectively rejected by the request of at least one point in the SPD, which has  
 78 a very limited time acquisition window (300 ns). Indeed, though the default associated track selection  
 79 requires a minimum of 2 points in the ITS, as it will be shown later on full compatibility of the corrected  
 80 results with 2 and 3 minimum ITS clusters is obtained. For FAST and CENT\_woSDD samples, the latter  
 81 case indirectly forces the presence of a point in the SPD.

82 Since data collected during p-Pb 2016 data taking are distinguished into two categories - one including  
 83 SDD detector (CENT\_wSDD sample) and a second one without the SDD in the reconstruction, or in the  
 84 acquisition (CENT\_woSDD and FAST samples, respectively), a study of performance of the D-hadron  
 85 correlation analysis with respect to the data samples employed has been carried out for  $D^{*+}$  and  $D^+$   
 86 mesons (more sensitive to the presence of the SDD w.r.t. the  $D^0$ , due to their reconstruction from three  
 87 decay tracks).

88 For this reason, the D-hadron correlation distribution has been compared on LHC16q\_pass1\_CENT\_wSDD  
 89 and LHC16q\_pass1\_CENT\_woSDD and the relative statistical uncertainty has been estimated in order to  
 90 understand if it was better to perform the analysis separately on the two data sample, applying in this  
 91 case different corrections, or not. In particular, it was crucial for the correlation analysis involving the

Type	Production	Run list	nEvents
Monte-Carlo	LHC17d2a_fast_new (c/b enriched), LHC17a2b_fast (MB), LHC17a2b_cent_woSDD (MB)	267166, 267165, 267164, 267163, 265525, 265521, 265501, 265500, 265499, 265435, 265427, 265426, 265425, 265424, 265422, 265421, 265420, 265419, 265388, 265387, 265385, 265384, 265383, 265381, 265378, 265377, 265344, 265343, 265342, 265339, 265338, 265336, 265335, 265334, 265332, 265309 = [36 runs]	50M
Data	LHC16q, pass1_CENT_woSDD	265525, 265521, 265501, 265500, 265499, 265435, 265427, 265426, 265425, 265424, 265422, 265421, 265420, 265419, 265388, 265387, 265385, 265384, 265383, 265381, 265378, 265377, 265344, 265343, 265342, 265339, 265338, 265336, 265335, 265334, 265332, 265309 = [32 runs]	261M total
	LHC16q, pass1_FAST	265525, 265521, 265501, 265500, 265499, 265435, 265427, 265426, 265425, 265424, 265422, 265421, 265420, 265419, 265388, 265387, 265385, 265384, 265383, 265381, 265378, 265377, 265344, 265343, 265342, 265339, 265338, 265336, 265335, 265334, 265332, 265309 = [32 runs]	260M
	LHC16t, pass1_CENT_woSDD	267166, 267165, 267164, 267163 = [4 runs]	40M
	LHC16t, pass1_FAST	267166, 267165, 267164, 267163 = [4 runs]	41M

**Table 1:** Data Set and Run list

92 D<sup>\*+</sup> meson because the efficiency tracking reconstruction of the soft pion is  $\approx 10\%$  higher employing  
 93 also the SDD information. Figure 1 shows the normalized azimuthal correlation distribution for low, mid  
 94 and high  $p_T$  for D<sup>\*+</sup> meson. Blue points are referred to the woSDD sample while red points represents  
 95 wSDD data. Figure 2 shows the relative statistical uncentainty extracted from the azimuthal correlation  
 96 distributions for the D<sup>\*+</sup> in different kinematic ranges.

97 It can be observed that the data sample that includes the SDD information is characterized by  $\approx 10 - 15\%$   
 98 more statistics in each  $p_T$  ranges analyzed. This difference is related to the larger efficiency in track  
 99 reconstruction with the wSDD sample - a larger number of tracks survives to the selection request of 3  
 100 tracks in the ITS, which is part of the selection requests applied on the previous D-h analysis.

101 As a result, the wSDD sample is also affected by a slightly lower relative statistical uncertainty (about  
 102 12-15%) due to several reasons: the larger tracking efficiency, the major number of signal entries in the  
 103 invariant mass distributions and a slight increase of S/B, which reflects in a slight decrease of uncertainty  
 104 from the sideband subtraction. It has also to be considered that, on the full sample including also the  
 105 FAST cluster, the increase in performance would be further reduced. The overall statistical uncertainty  
 106 difference resulting from the comparison is not enough to justify the implementation of two different  
 107 analysis and two subsequent different corrections either for D<sup>\*+</sup> and D<sup>+</sup>.

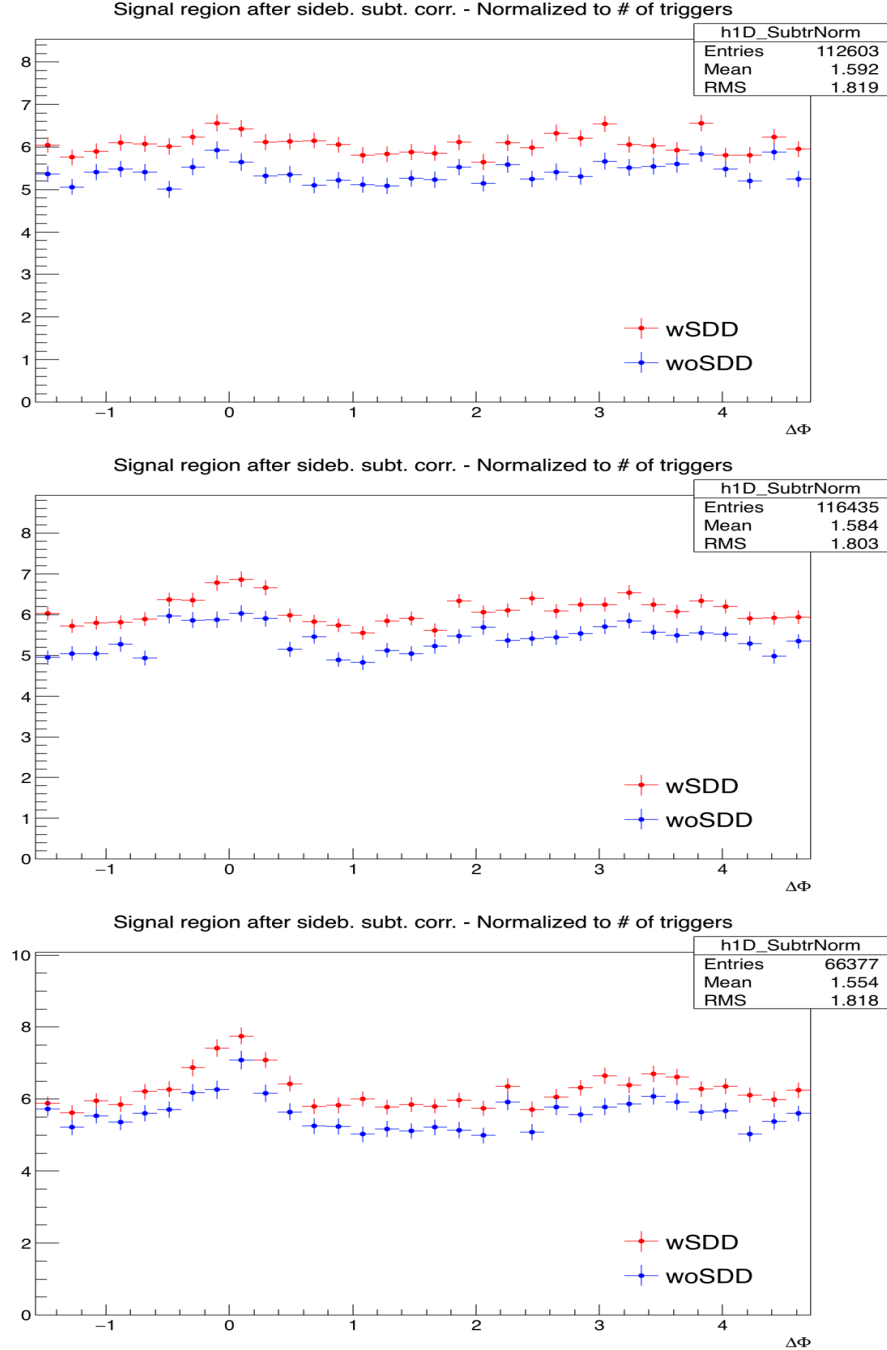


**Figure 1:** Normalized azimuthal correlation distribution of  $D^{*+}$  for low  $p_T$  ( $3 < p_T(D^{*+}) < 5 \text{ GeV}/c$ ) on the top panel, mid  $p_T$  ( $5 < p_T(D^{*+}) < 8 \text{ GeV}/c$ ) on the middle panel and high  $p_T$  ( $8 < p_T(D^{*+}) < 16 \text{ GeV}/c$ ) on the bottom panel with a  $p_T$  threshold for associated tracks of  $p_T(\text{assoc}) > 0.3 \text{ GeV}/c$ . Blu points are referred to the woSDD sample while red points represent wSDD data.

108 Anyway, to cope with the lower tracking efficiency w.r.t. 2013 data sample, after this study it was decided  
 109 to reduce the ITS request for the associated tracks from 3 (used on 2013 data) to 2 ITS clusters ad default  
 110 selection criterion.

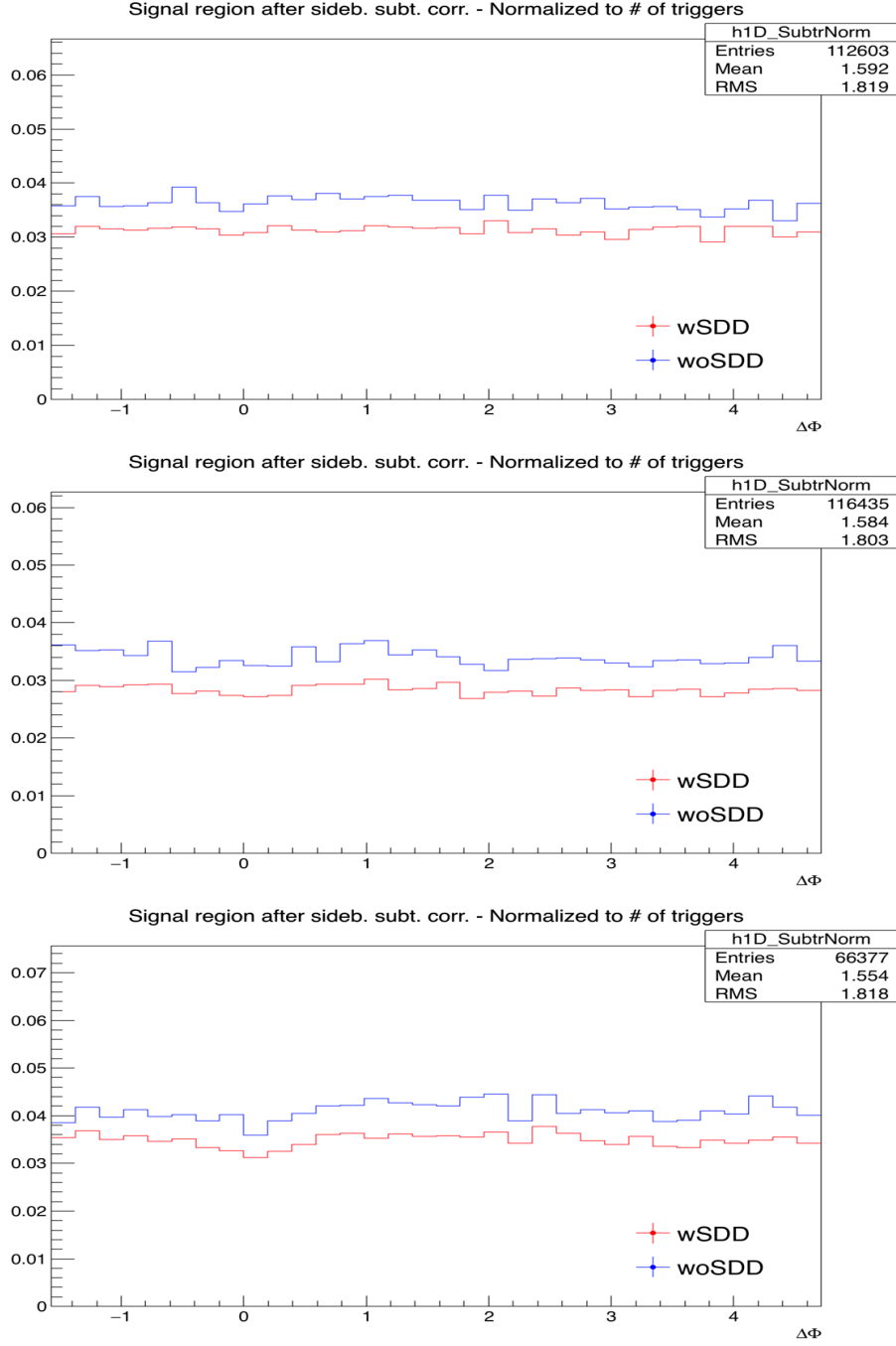


**Figure 2:** Statistical uncertainty extracted from the azimuthal correlation distribution of  $D^{*+}$  with associated charged particles. Top panel:  $3 < p_T(D^{*+}) < 5 \text{ GeV}/c$ . Mid panel:  $5 < p_T(D^{*+}) < 8 \text{ GeV}/c$ . Bottom panel:  $8 < p_T(D^{*+}) < 16 \text{ GeV}/c$ . Blue line is referred to the woSDD sample while the red line represents wSDD data.

### 111 3 Analysis strategy

112 The analysis strategy follows the one used from 2013 p-Pb data sample. Correlation pairs are formed by  
 113 trigger particles (D mesons) reconstructed and selected in the following  $p_T^{\text{trig}}$  ranges:  $3 < p_T^{\text{trig}} < 5 \text{ GeV}/c$ ,  
 114  $5 < p_T^{\text{trig}} < 8 \text{ GeV}/c$ ,  $8 < p_T^{\text{trig}} < 16 \text{ GeV}/c$ ,  $16 < p_T^{\text{trig}} < 24 \text{ GeV}/c$ , and associated particles (charged  
 115 tracks) for the following  $p_T^{\text{assoc}}$  regions:  $p_T^{\text{assoc}} > 0.3$ ,  $0.3 < p_T^{\text{assoc}} < 1$ ,  $1 < p_T^{\text{assoc}} < 2$ ,  $2 < p_T^{\text{assoc}} < 3$ ,  
 116  $p_T^{\text{assoc}} > 3 \text{ GeV}/c$  (with the addition of  $p_T^{\text{assoc}} > 1 \text{ GeV}/c$  for comparison with p-Pb 2013 results). In  
 117 D meson correlations, the particle identification defines the trigger particle rather than a momentum cut

118 and therefore the momentum range of the associated particles is not constrained by that of the trigger  
 119 particle. Our definition of associated particle includes any charged particle coming from the primary  
 120 vertex of interaction, including those coming from strong and electromagnetic decay of unstable parti-  
 121 cles, and particles deriving from the decay of hadrons with charm or beauty. We therefore include any  
 122 charged particle except those coming from weak decays of strange particles and particles produced in the  
 123 interaction with the detector material. This definition corresponds to that used in the method AliAODM-  
 124 CParticle::IsPyphysicalPrimary(). All associated particles surviving the selection cuts and not matching  
 125 the adopted criterion are considered as a contamination whose contribution has to be corrected for.

126

127 The analysis is performed through the following steps:

- 128 1. **D meson selection and signal extraction.** For each single event, “trigger” particles are defined  
 129 as the selected D meson candidates ( $D^0$ ,  $D^+$  and  $D^{*+}$ ) within a given  $p_T^{\text{trig}}$  range. The detection  
 130 strategy for D mesons at central rapidity is the same performed for the analyses of the D-meson  
 131 production at central rapidity [1], and also applied for the D-h analysis on 2010 pp and 2013 p-Pb  
 132 samples [2] and is based on the reconstruction of decay vertices displayed from the primary vertex  
 133 by a few hundred  $\mu\text{m}$  and on the identification of the decay-particle species. The identification of  
 134 the charged kaon and pion in the TPC and TOF detectors helps to further reduce the background at  
 135 low  $p_T$ . An invariant-mass analysis is then used to extract the raw signal yield, using the same fit  
 136 functions described in [2]. The D mesons are selected in the rapidity range varying from  $|y| < 0.5$   
 137 at low  $p_T$  to  $|y| < 0.8$  for  $p_T > 5 \text{ GeV}/c$ .
- 138 2. **Correlation of D candidates with associated tracks.** Particle pairs are formed by associating each  
 139 trigger particle with the charged primary particles passing the track selection (excluding those  
 140 coming from the decay of the D-meson candidate) in a specified  $p_T^{\text{assoc}}$  interval (which can overlap  
 141 with the  $p_T^{\text{trig}}$  range) and in the pseudo-rapidity range  $|\eta| < 0.8$ . For the  $D^0$  meson, also the low-  
 142 momentum pion tracks from feed-down of  $D^{*+}$  mesons are removed via  $3\sigma$  invariant mass cut on  
 143 the  $M(K\pi\pi) - M(K\pi)$  difference. This because these soft pion are not related to the charm quark  
 144 fragmentation chain. For D meson candidates in the invariant mass signal region, defined by a  $\pm$   
 145  $2\sigma$  interval around the D meson mass, the azimuthal angle difference  $\phi^{\text{assoc}} - \phi^{\text{trigg}} \equiv \Delta\phi$  and the  
 146 pseudorapidity difference  $\eta^{\text{assoc}} - \eta^{\text{trig}} \equiv \Delta\eta$  are evaluated and stored to build two-dimensional  
 147 correlation distribution.
- 148 3. **Correction for limited acceptance and detector inhomogeneities with Event Mixing** The angular  
 149 correlation distribution may be affected, even for uncorrelated pair of particles, by structures  
 150 not due to physical effects, but originating from the limited detector acceptance, as well as from  
 151 angular inhomogeneities in the trigger and track reconstruction efficiencies as a function of  $\Delta\phi$   
 152 and  $\Delta\eta$ . Effects of this kind are removed using the Event Mixing technique. In this technique, the  
 153 analysis is executed on the same data sample of the standard one (called “same event” analysis,  
 154 SE), but the trigger particles found in each event are correlated to charged particles reconstructed  
 155 in different events (“Mixed Events” analysis, ME) with similar characteristic, in particular con-  
 156 cerning the event multiplicity and z position of the primary vertex (see Section 3.3.1).

157

158 The differential yield of associated particles per trigger particle is obtained by

$$\frac{1}{N_{\text{trig}}} \frac{d^2 N^{\text{pair}}}{d\Delta\eta d\Delta\phi} = B_{\text{ME}}(0, 0) \times \frac{S(\Delta\eta, \Delta\phi)}{B_{\text{ME}}(\Delta\eta, \Delta\phi)}, \quad (1)$$

159 where  $N^{\text{pair}}$  is the total number of correlated D-hadron pairs. The functions  $S(\Delta\eta, \Delta\phi)$  and  $B_{\text{ME}}(\Delta\eta, \Delta\phi)$   
 160 are the signal and the mixed event background distributions, respectively. The latter is normalized

to its value in  $(\Delta\eta, \Delta\phi) = (0, 0)$ , i.e.  $(B(0, 0))$ . Further details on the mixed-event correction are provided further on.

4. **Subtraction of background correlation from signal distribution.** The invariant mass signal region includes also background D-meson candidates. Their contribution to the raw correlation distribution is subtracted as follows. For each  $p_T$  bin, the mean and the sigma of the invariant mass spectrum are extracted. For  $D^0$  and  $D^+$ , a “background” region is defined in the sidebands of the mass distribution as the interval  $4\text{GeV}/c^2 < |m - m^{\text{pdg}}| < 8\text{GeV}/c^2$  (for the  $D^{*+}$  meson, only the right sideband is used). The angular correlation distribution for background candidates in this region is extracted and normalized with respect to the background in the signal region estimated from the mass fit. This normalized background correlation distribution is then subtracted from the raw signal one to obtain the signal correlation distribution. The normalization factor is the ratio of the number of background candidates under the signal peak (obtained by integrating the background of the fit function within the signal region) over the number of background candidates in the sidebands (obtained via bin-counting in the sideband region). This normalized background correlation distribution is then subtracted from the raw signal one to obtain the signal correlation distribution. An example of the signal region, sideband and sideband-subtracted 1D correlation distributions (along  $\Delta\phi$ ) is shown in figure 3, together with the comparison of the three distributions after the normalization to the number of triggers.

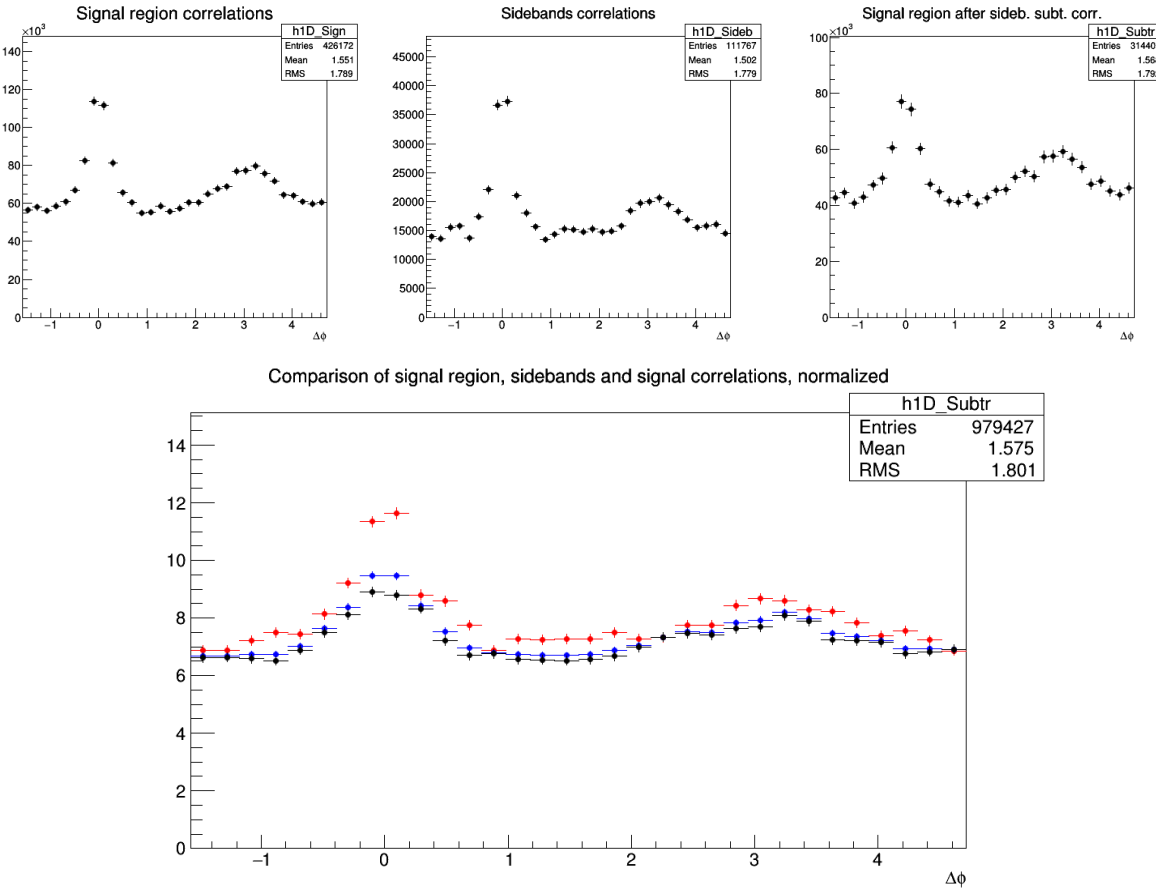


**Figure 3:** Top: Example of  $D^0$ - $h$  signal region (left), sideband (middle), and signal minus sideband (right) correlation distributions. Bottom: signal region per-trigger normalized correlation distribution (blue), sideband region per-trigger normalized correlation distribution (red), background-subtracted per-trigger normalized correlation distribution (black).

5. **Correction for D meson efficiency and associated track efficiency.** After filling the signal and

background correlation distributions, it is necessary to take into account also for the correlations with tracks not reconstructed, or not passing the quality selection due to poor reconstruction. In the same way, the loss of D-mesons which are not reconstructed, or do not pass the selection, impacts the correlation distribution shape. Hence, each pair is weighted by the inverse of the product of the associated track and D meson reconstruction efficiency,  $\epsilon_{trk}$  and  $\epsilon_{trig}$ . Further details are provided later on in this section.

6. **Projection in  $\Delta\phi$ .** The limited statistics available does not allow to study the two dimensional  $(\Delta\eta, \Delta\phi)$  distribution, which is therefore projected to the  $\Delta\phi$  axis by integrating on  $|\Delta\eta| < 1$ . Despite, in principle, our maximum  $\Delta\eta$  acceptance is of  $|\Delta\eta| < 1.6$ , removing the large  $|\Delta\eta|$  regions allow us to reject angular regions with very low statistics, where fluctuations would be amplified by a large mixed-event correction, and avoid the so-called wings effect.

As the difference in the azimuthal angle is periodic ( $\Delta\phi = 0 = 2\pi$ ), the  $\Delta\phi$ -range is limited to the essential range of  $2\pi$ . The  $\Delta\phi$ -limits are chosen to be  $[-\pi/2, 3\pi/2]$  in order to provide a good visibility of the correlation pattern, which peaks around 0 and  $\pi$ .

7. **Correction for the contamination of secondary particles** The DCA to primary vertex cut, applied during the associated track selection, has the role of removing the secondary particles from the associated track sample. Secondary particles are indeed produced either from long-lived strange hadrons or from interaction of particles with the detector material. A residual contamination from secondary tracks is hence expected in the correlation distributions. This contamination is estimated from Monte Carlo simulation based on Pythia as described more in detail in the next section. The background-subtracted event-mixing corrected correlations are multiplied by a purity factor to remove this contribution.

8. **Correction for feed-down of D meson from b-hadron decay** The selection strategy employed for the D meson candidates selection enhances the fraction of reconstructed D mesons coming from the decay of a b-hadron. Typical values, with the cuts used for the D-meson selection, are of the order of 10% or less. The correlation distribution of these secondary D mesons will be sensitive to the properties of beauty jets and beauty hadron decay, which in general differ from those relative to charm jets and hadrons. The procedure used to subtract this contribution is described in the next paragraphs of this section.

9. **Study of correlation properties.** The properties of the azimuthal correlation distribution are quantified by fitting the distribution with a function composed of two Gaussian functions, modelling the near and the away side peaks, and a constant term describing the baseline. The mean of the Gaussian are fixed at  $\Delta\phi = 0$  and  $\Delta\phi = \pi$ . To accomplish the  $2\pi$  periodicity of the  $\Delta\phi$  variable, the Gaussian functions are “duplicated” with mean at  $\Delta\phi = 2\pi$  and  $\Delta\phi = -\pi$ . The fitting procedure is described in details in Section 5.

### 3.1 Mass plots and cut optimization

The invariant mass distributions in the various  $p_T$  ranges studies are shown in Figure 4, 5 and 6 for  $D^0$ ,  $D^{*+}$  and  $D^+$  respectively.

For  $D^{*+}$ , the standard D2H p-Pb cuts (for the 2013 cross section analysis) were used. The same holds for the  $D^+$ , but with the addition of cuts on the normalized decay length in  $xy$  plane and of the normalized difference between measured and expected daughter track impact parameters (topomatic cut). A particular cut optimization was instead performed for the  $D^0$  meson. Twelve cut sets were tried, with the goal of increasing the S/B factor, in order to reduce fluctuations induced by the sideband subtraction (the limiting factor for the analysis performance). In Figure 7 the  $D^0$ -h correlation distributions are shown for the different cut sets, in exemplary kinematic regions (left column), together with the bin-by-bin relative

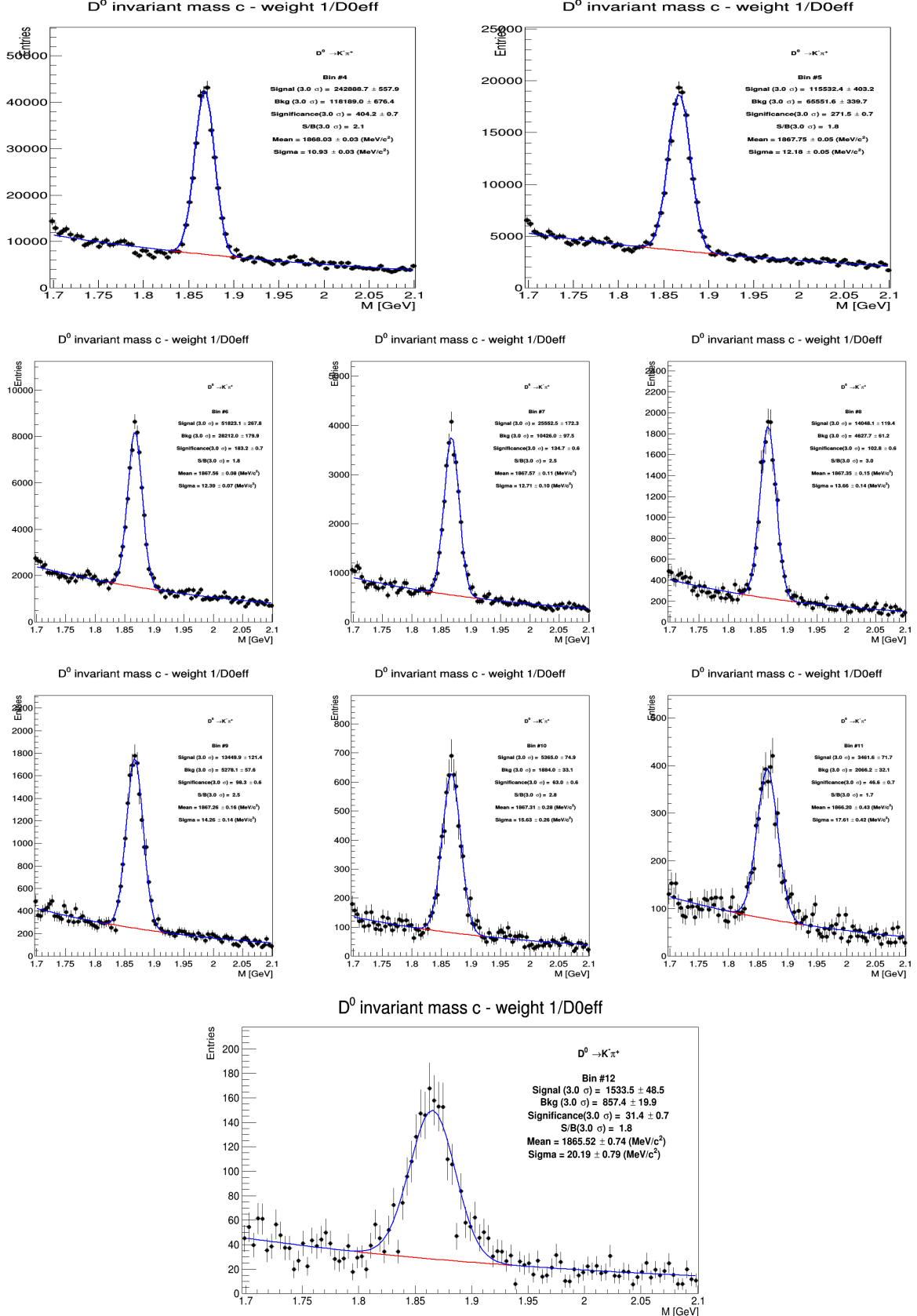


**Figure 4:** Invariant mass distributions of  $D^0$  in different  $p_T^D$  regions. Top:  $3 < p_T^D < 4$  GeV/c (left),  $4 < p_T^D < 5$  GeV/c right), Mid 1:  $5 < p_T^D < 6$  GeV/c (left),  $6 < p_T^D < 7$  GeV/c (middle),  $7 < p_T^D < 8$  GeV/c (right); Mid2:  $8 < p_T^D < 10$  GeV/c,  $10 < p_T^D < 12$  GeV/c (middle),  $12 < p_T^D < 16$  GeV/c (right) and Bottom:  $16 < p_T^D < 24$  GeV/c.

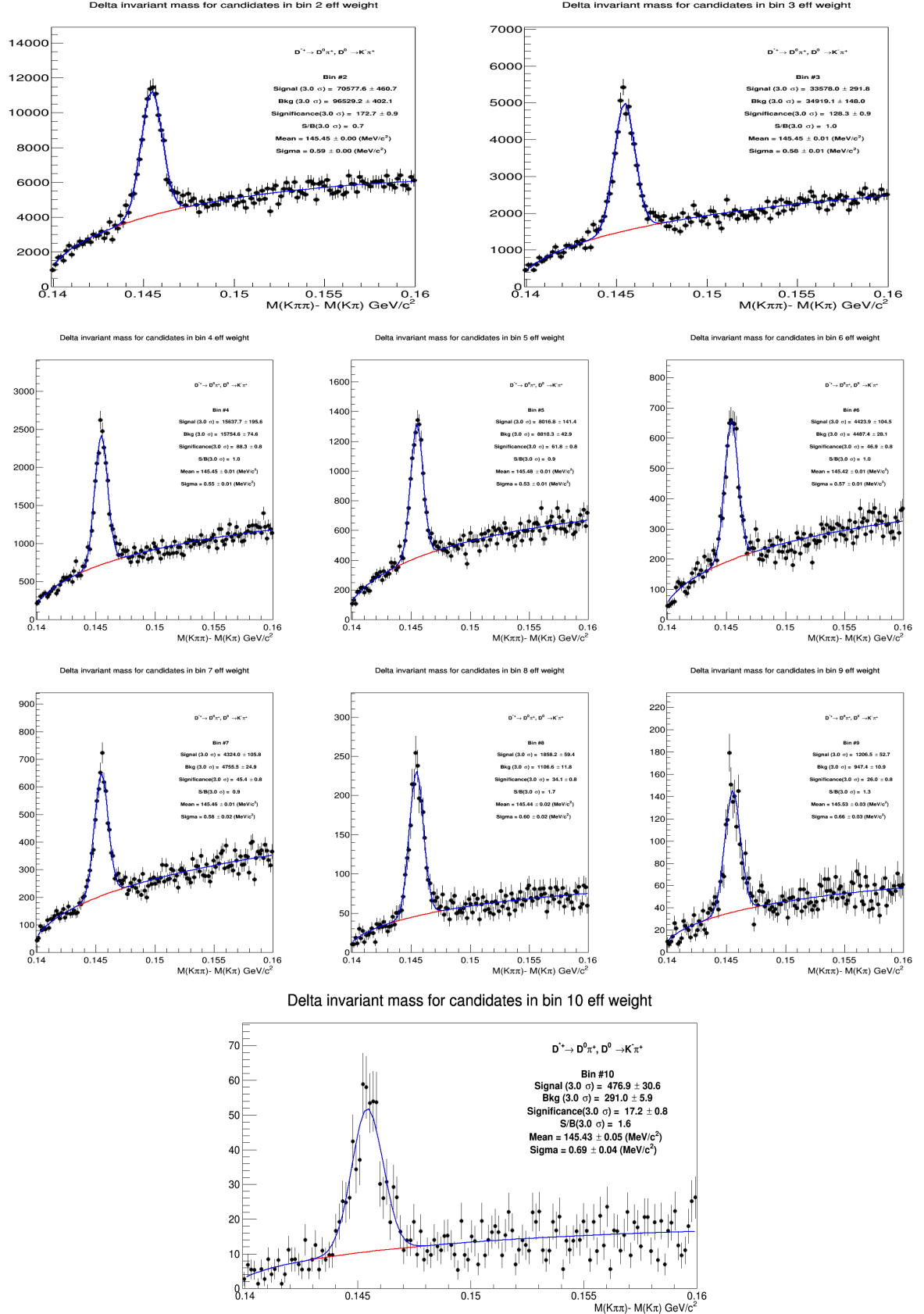


**Figure 5:** Invariant mass distributions of  $D^{*+}$  in different  $p_T$  regions. Top:  $3 < p_T^D < 4$  GeV/c (left),  $4 < p_T^D < 5$  GeV/c (right), Mid 1:  $5 < p_T^D < 6$  GeV/c (left),  $6 < p_T^D < 7$  GeV/c (middle),  $7 < p_T^D < 8$  GeV/c (right); Mid2:  $8 < p_T^D < 10$  GeV/c,  $10 < p_T^D < 12$  GeV/c (middle),  $12 < p_T^D < 16$  GeV/c (right) and Bottom:  $16 < p_T^D < 24$  GeV/c .

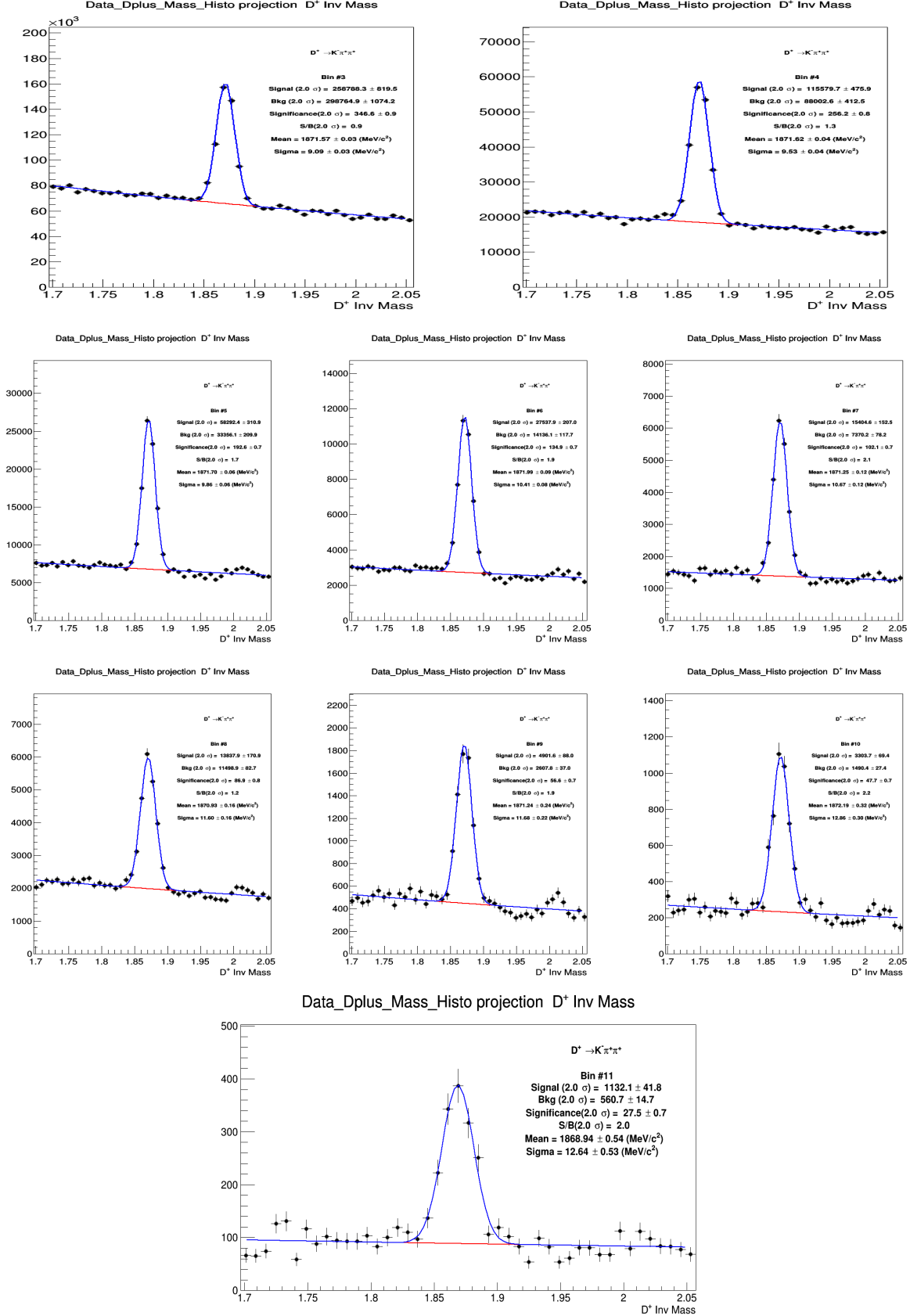


**Figure 6:** Invariant mass distribution of  $D^+$  in different  $p_T$  regions. Top:  $3 < p_T^D < 4$  GeV/c (left),  $4 < p_T^D < 5$  GeV/c right), Mid 1:  $5 < p_T^D < 6$  GeV/c (left),  $6 < p_T^D < 7$  GeV/c (middle),  $7 < p_T^D < 8$  GeV/c (right); Mid2:  $8 < p_T^D < 10$  GeV/c,  $10 < p_T^D < 12$  GeV/c (middle),  $12 < p_T^D < 16$  GeV/c (right) and Bottom:  $16 < p_T^D < 24$  GeV/c .

statistical uncertainty on the data points (right column). The best cut set (option G) was defined from the standard cuts used for the p-Pb 2013 cross section analysis, with a tightened selection on the cosine of the pointing angle, and with the addition of a cut on the normalized decay length in  $xy$  plane and of a selection on the normalized difference between measured and expected daughter track impact parameters (topomatic cut).

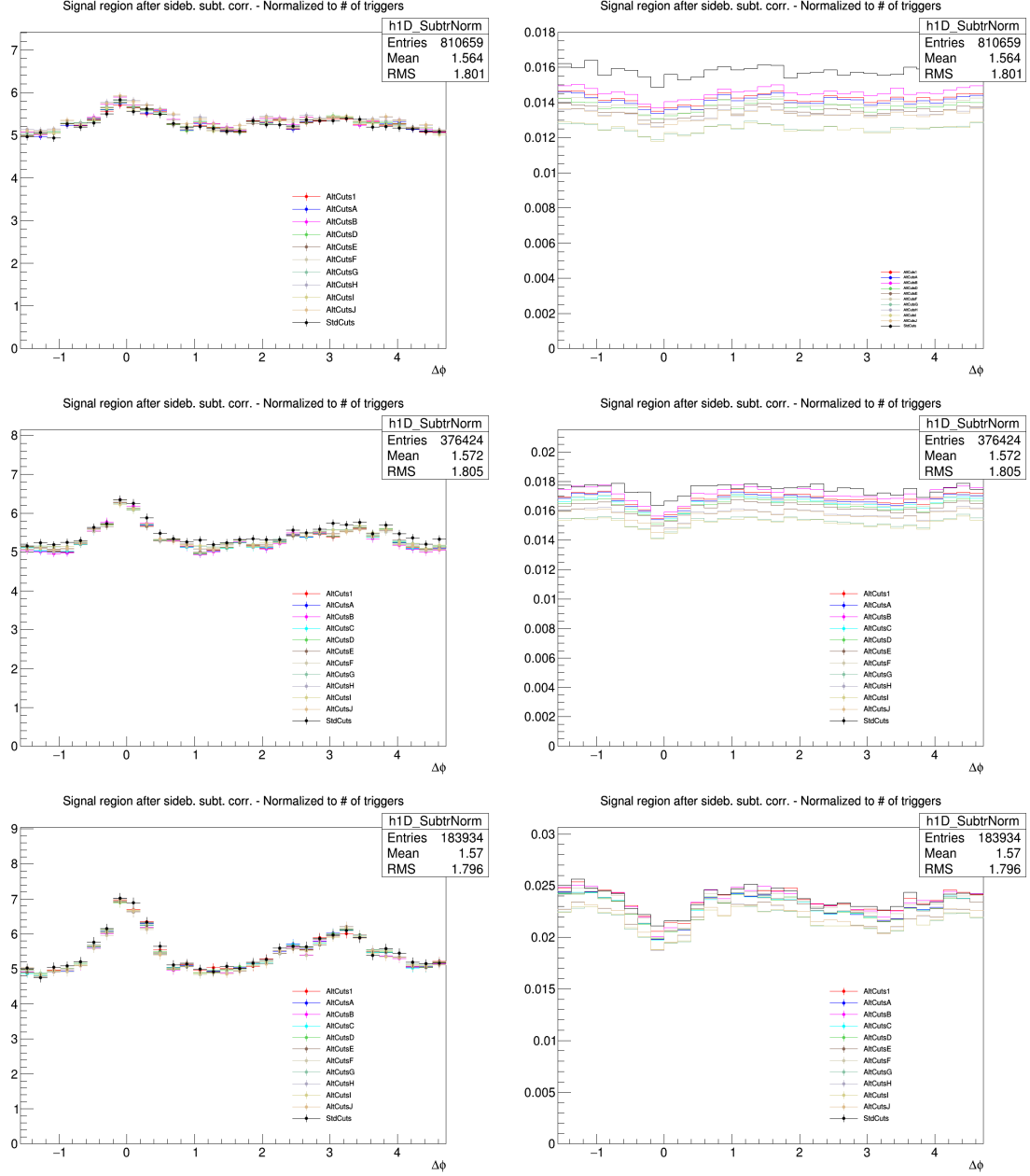


**Figure 7:**  $D^0$ - $h$  correlation distributions with different cut options (left) and point-by-point relative statistical uncertainty (right) for  $3 < p_T^D < 5 \text{ GeV}/c$  (top),  $5 < p_T^D < 8 \text{ GeV}/c$  (middle),  $8 < p_T^D < 16 \text{ GeV}/c$  (bottom), in all cases with associated track  $p_T > 0.3 \text{ GeV}/c$ .

### 3.2 Code used for the analysis

The code used for D meson-hadron correlation analysis is fully committed in AliPhysics. The analysis classes can be found in `$ALICE_ROOT/PWGHF/correlationHF/`. The D meson specific classes where the aforementioned steps are carried out are `AliAnalysisTaskDStarCorrelations`, `AliAnalysis-`

234 TaskSED0Correlations and AliAnalysisTaskDplusCorrelations. The classes which are common to the D  
 235 meson specific analysis which includes the associated particle cuts and the correlation observables are Al-  
 236 iHFAssociatedTrackCuts, AliHFCorrelator, AliHFOfflineCorrelator, AliReducedParticle and AliDhCor-  
 237 relationExtraction. Several additional classes and macros in the same folder deal with the correction  
 238 steps.

239 **3.3 Further details on corrections**

240 **3.3.1 Event Mixing**

241 The event-mixing technique is used for correcting the raw correlation distribution for effects arising  
 242 from the detector limited acceptance in rapidity and detector spatial inhomogeneities. The calculation  
 243 of the Event Mixing correlation distribution is performed online. An event pool is created, where events  
 244 preceding the one containing a D candidate are stored based on their properties (position of the vertex  
 245 along the z axis and multiplicity). Each time a D meson candidate is found in an event, only the events  
 246 contained in the same pool as the event under analysis is used to evaluate the correlations for the event  
 247 mixing correction.

248 For  $D^0$  and  $D^+$ , an offline approach for the mixed-event correction has been developed. In this approach,  
 249 D-meson triggers and associated tracks from every analyzed event are stored in dedicated TTree, together  
 250 with the needed kinematic information to build correlation distributions, and with identifiers of the events  
 251 to which they belong. In this way, it is possible to correlate each D meson with all the tracks belonging  
 252 to the same pool over the full event sample, and not being limited to the same subjob as for the online  
 253 analysis. This allows to increase the statistics of the mixed-event correlation distributions. It was verified  
 254 that online and offline approaches are fully compatible within the statistical uncertainties.

255 The multiplicity and z vertex position bins for the pools used in the p-Pb analysis (for both approaches)  
 256 are the following:

- 257 – Multiplicity bins:  $(0, 40); (40, 65); (65, +\infty)$  (THESE ARE BEING SLIGHTLY CHANGED)
- 258 – Vertex z (cm) =  $(-10, -2.5); (-2.5, 2.5); (2.5, 10)$  (THESE ARE BEING SLIGHTLY CHANGED)

259 In an ideal case, the mixed event distribution is expected to have a constant flat distribution as function  
 260 of  $\Delta\phi$  and a triangular shaped distribution in  $\Delta\eta$  deriving from the limited  $\eta$  acceptance of the detector.  
 261 In case, instead of detector inefficient regions, or holes, in the same angular position for D meson and  
 262 associated tracks, these structures produce an excess of correlations at  $\Delta\phi = 0$  in the  $\Delta\phi$  distribution. The  
 263 obtained distribution is used as a weight in each correlation bin, i.e, the corrected correlation distribution  
 264 is calculated as follows:

$$\frac{dN^{corr}(\Delta\phi\Delta\eta)}{d\Delta\phi d\Delta\eta} = \frac{\frac{dN^{SE}(\Delta\phi\Delta\eta)}{d\Delta\phi d\Delta\eta}}{\frac{dN^{ME}(\Delta\phi\Delta\eta)}{d\Delta\phi d\Delta\eta}} \frac{dN^{ME}(0,0)}{d\Delta\phi d\Delta\eta} \quad (2)$$

265 In the previous equation, the last term stands for the average of the bins in the region  $-0.2 < \Delta\eta < 0.2$ ,  
 266  $-0.2 < \Delta\phi < 0.2$  (multiple bins are used to minimize the effect of statistical fluctuations on the normal-  
 267 ization of the mixed-event plots). This kind of normalization, adopted in the analysis of hadron-hadron  
 268 correlations, relies on the fact that at  $(\Delta\eta, \Delta\phi) = (0, 0)$  the trigger and associated particle experience  
 269 the same detector effects. In the D meson case this is true only on average and not at very low  $p_T$ ,  
 270 since D mesons are reconstructed from particles that can go in different detector region. However,  
 271  $(\Delta\eta, \Delta\phi) = (0, 0)$  is in any case the region with maximum efficiency for the pairs (both correlated and  
 272 uncorrelated). Thus the same convention was adopted.

273 The mixed-event correlation distributions are built in both D meson signal and sideband regions. Both  
 274 are corrected with the relative distributions. An example of the mixed-event distributions, and of the

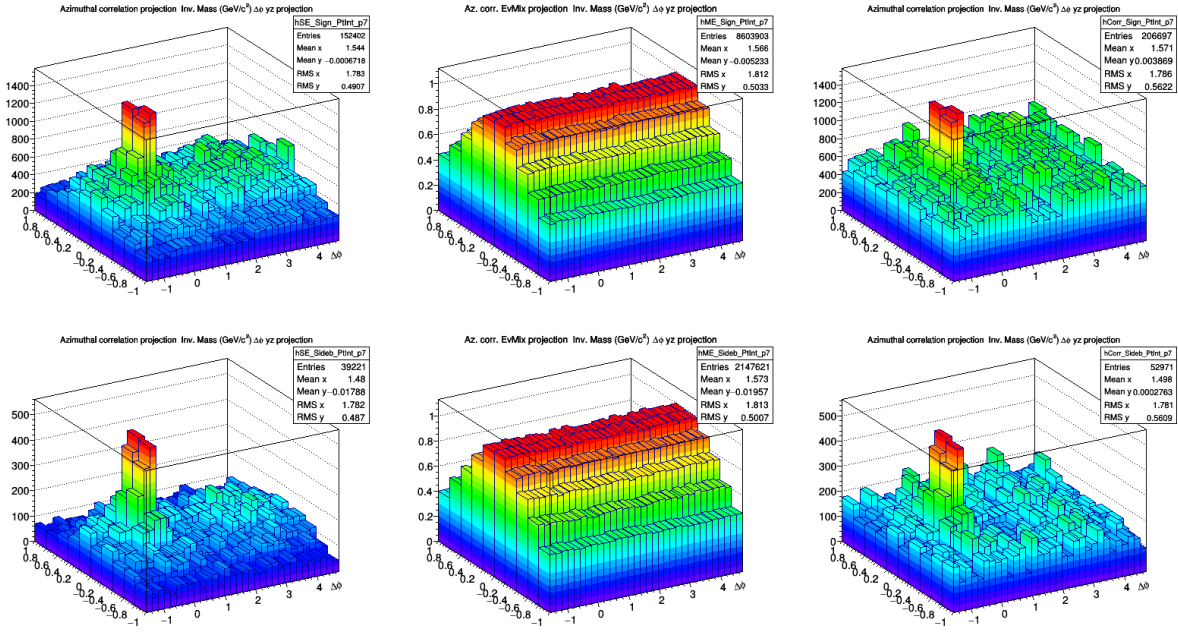


**Figure 8:**  $D^0$  meson ( $\Delta\phi, \Delta\eta$ ) correlation for in the signal region (top row) and sidebands (bottom row) from Single Event (left) and Mixed Event analysis (center) for high  $p_T$ :  $8 < p_T < 16$  GeV/c with associated  $p_T < 0.3$  GeV/c. The right column shows the SE/ME corrected distributions.

275 outcome of the mixed-event correction, is provided in Figures 8 and ???. The expected triangular shape  
 276 in  $\Delta\eta$ , for the mixed-event distributions, addresses the effect of the limited detector pseudo-rapidity  
 277 acceptance. Note that the mixed-event distribution is limited to the interval  $|\Delta\eta| < 1$ : the decision to  
 278 limit the mixed-event correction, and thus the whole analysis, to this range was taken in order to avoid  
 279 the so-called “wing effect”, i.e. the wing-like structures arising in the correlation distribution at large  $\Delta\eta$   
 280 due to the limited filling of the correlation bins in that region.

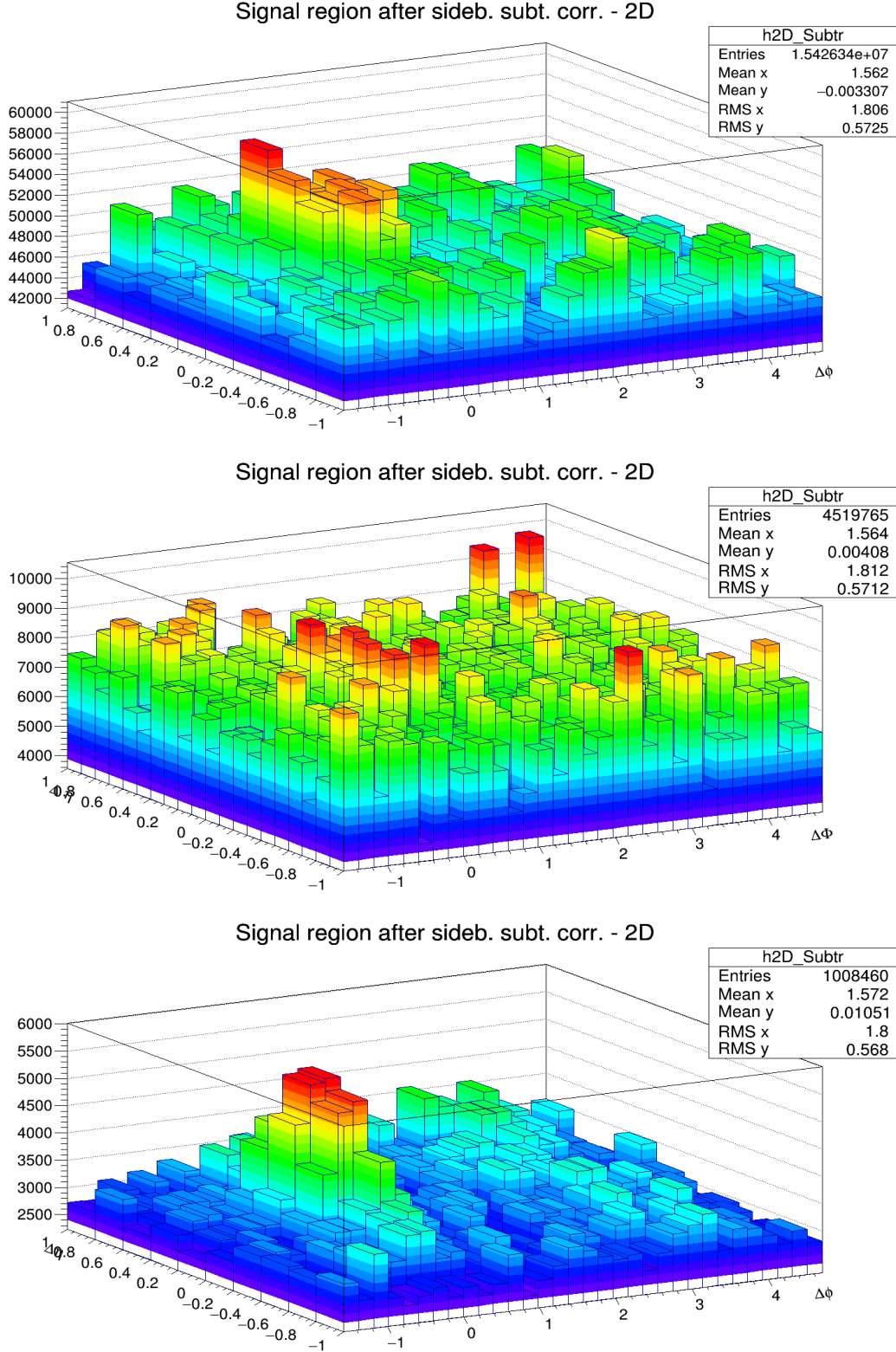


**Figure 9:** Top:  $(\Delta\phi, \Delta\eta)$  correlation distribution of  $D^0$ -h with  $3 < p_T < 5$  GeV/c and associated track kinematic range:  $0.3 < p_T < 1.0$  GeV/c Mid:  $(\Delta\phi, \Delta\eta)$  correlation distribution of  $D^{*+}$ -h with  $3 < p_T < 5$  GeV/c and associated track  $p_T$  Threshold:  $p_T > 0.3$  GeV/c Bottom:  $(\Delta\phi, \Delta\eta)$  correlation distribution of  $D^+$ -h with  $8 < p_T < 16$  GeV/c and associated track  $p_T$  threshold:  $p_T > 0.3$  GeV/c. All the plots are shown after the mixed-event correction and the sideband subtraction.

281 **3.3.2 Tracking and D-meson trigger efficiency**

282 **(i) Tracking efficiency** - The tracking efficiency was calculated by obtaining the ratio between the yield  
 283 at the reconstructed level and generated level, for a defined “type” of particles (in our case non-identified  
 284 particles) and it is estimated differentially in  $p_T$ ,  $\eta$ , and  $z_{vtx}$  of the event.

285

286 Tracking efficiency maps were produced as TH3D histograms ( $p_T$ ,  $\eta$ ,  $z_{vtx}$ ) obtained from MC analysis on  
 287 the minimum-bias samples LHC17a2b\_fast and LHC17a2b\_cent\_woSDD, and applying at reconstructed  
 288 level the track selections (summarized in Table. 2). These efficiency maps were used in the analysis  
 289 tasks to extract single track efficiencies; each correlation pairs found in the data analysis was inserted  
 290 in correlation plots with a weight of **1/efficiency value**. Plots of the  $p_T$  dependence of the tracking  
 291 efficiency for two different track selections are shown in Fig. 10.

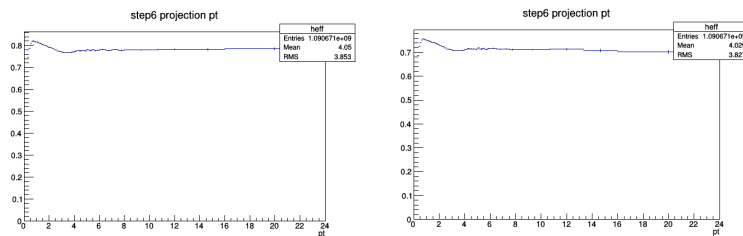


**Figure 10:**  $p_T$  efficiency map for standard track selection (2 ITS clusters) on top panel, and alternate track selection, used for systematics (3 ITS clusters, filterbit4, ITS refit) on bottom panel.

292 Details of cuts at event level and particle selection at different steps are listed in Table 2 .

<b>MC Generated</b>	
Stages	Cuts
1. MC Part with Generated Cuts	<b>After Event Selection</b> Charge PDG Code Physical Primary <b>Kinematics Cuts</b> $-0.8 < \eta < 0.8$ $pT > 0.3 \text{ (GeV}/c)$
2. MC Part with Kine Cuts	
<b>MC Reconstructed</b>	
4. Reco tracks	<b>After Event Selection</b> Physical Primary <b>Kinematics Cuts</b> $-0.8 < \eta < 0.8$ $pT > 0.3 \text{ (GeV}/c)$
5. Reco tracks with Kine Cuts	
6. MC true with Quality Cuts	<b>Quality Cuts</b> SetRequireSigmaToVertex(kFALSE) SetDCAToVertex2D(kFALSE) SetMinNCrossedRowsTPC(70) SetMinRatioCrossedRowsOverFindableClustersTPC(0.8) SetMinNClustersITS(2) SetMaxChi2PerClusterTPC(4) SetMaxDCAToVertexZ(1) SetMaxDCAToVertexXY(1) SetRequireTPCRefit(TRUE) SetRequireITSRefit(FALSE)
7. Reco tracks with Quality Cuts	<b>Same as step 6</b>

Table 2: Single Track Efficiency cuts detail

293  
 294 **(ii) D Meson efficiency** - Due to limited statistics, the correlation analysis is performed in quite wide  $p_T$   
 295 bins and in each of them the reconstruction and selection efficiency of D mesons is not flat, in particular  
 296 in the lower  $p_T$  region. We correct for the  $p_T$  dependence of the trigger efficiency within each  $p_T$ -bin.

297 This correction is applied online, by using a map of D meson efficiency as a function of  $p_T$  and event  
 298 multiplicity (in terms of SPD tracklets in  $|\eta| < 1$ ) extracted from the enriched Monte Carlo sample  
 299 LHC17d2a\_fast\_new. The  $\eta$  dependence was neglected due to the statistics of the available Monte Carlo  
 300 sample, which avoided the possibility of performing a 3D study.

301 To properly count the number of trigger particles used to normalize the correlation distributions,  $N_{\text{trig}}$ ,  
 302 each D meson is weighted with the inverse of its efficiency in the invariant mass distribution. The main  
 303 role of the correction for the D meson efficiency is to account for the  $p_T$  dependence of the correlation  
 304 distribution within a given D meson  $p_T$  interval. Indeed, only the  $p_T$  shape of the D meson efficiency  
 305 within the correlation  $p_T^{\text{trig}}$  ranges is relevant while the average value in the  $p_T$  range is simplified due to  
 306 the normalization of the correlation distribution to the number of trigger particles.

307 It was observed that multiplicity dependence of the efficiency does not bias the extraction of the signal  
 308 yield from the invariant mass distributions (which, as anticipated, are also weighted in the same manner).  
 309 Efficiency plots for  $D^0$ ,  $D^+$  and  $D^{*+}$  mesons are shown in Figs. 11 and 12.

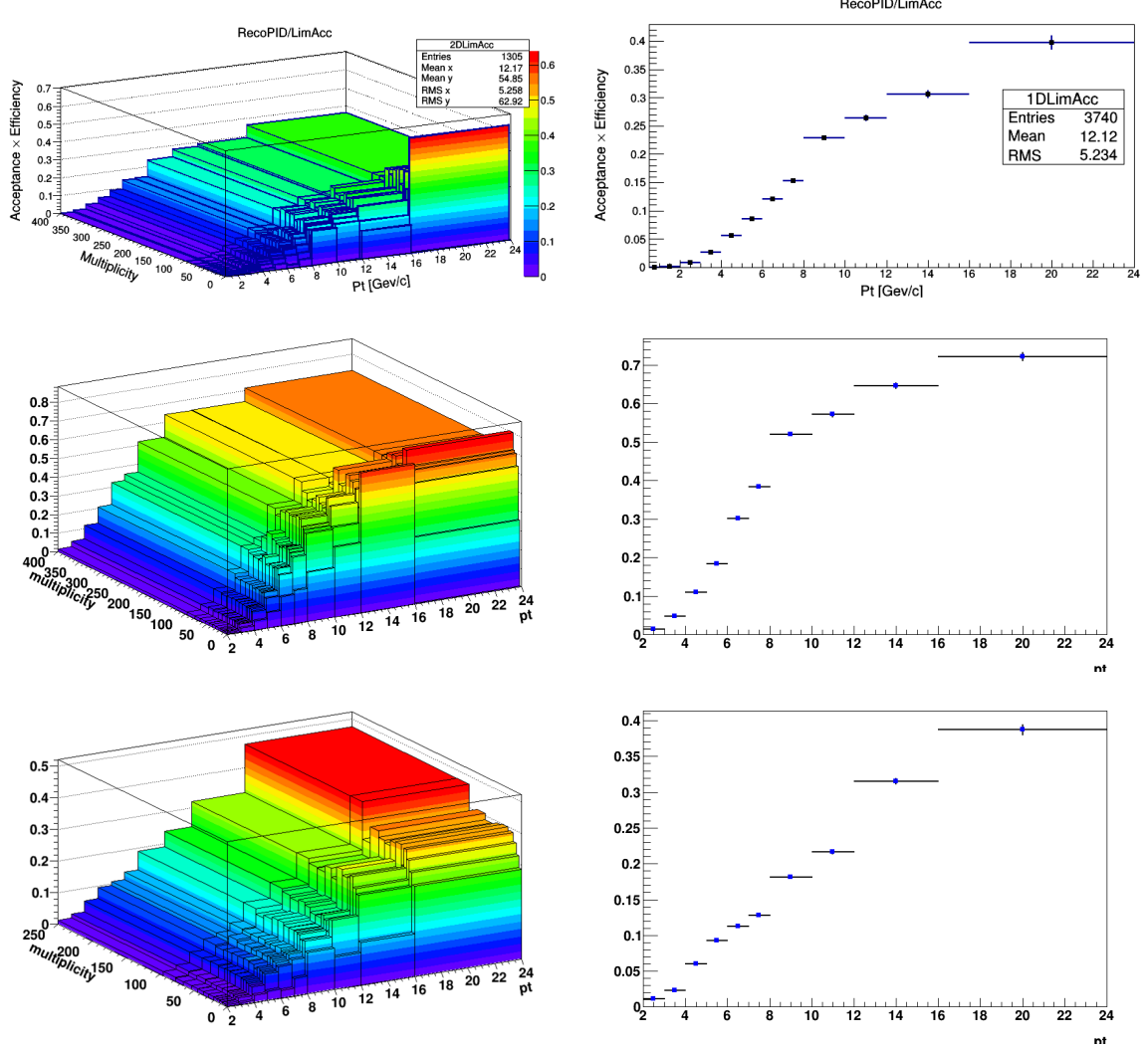


**Figure 11:** Top panel: ( $p_T$ , multiplicity) dependence (left) and  $p_T$  dependence (right) of prompt  $D^+$  meson efficiency. Mid panel: ( $p_T$ , multiplicity) dependence (left) and  $p_T$  dependence (right) of prompt  $D^{*+}$  meson efficiency. Bottom panel: ( $p_T$ , multiplicity) dependence (left) and  $p_T$  dependence (right) of prompt  $D^0$  meson efficiency.

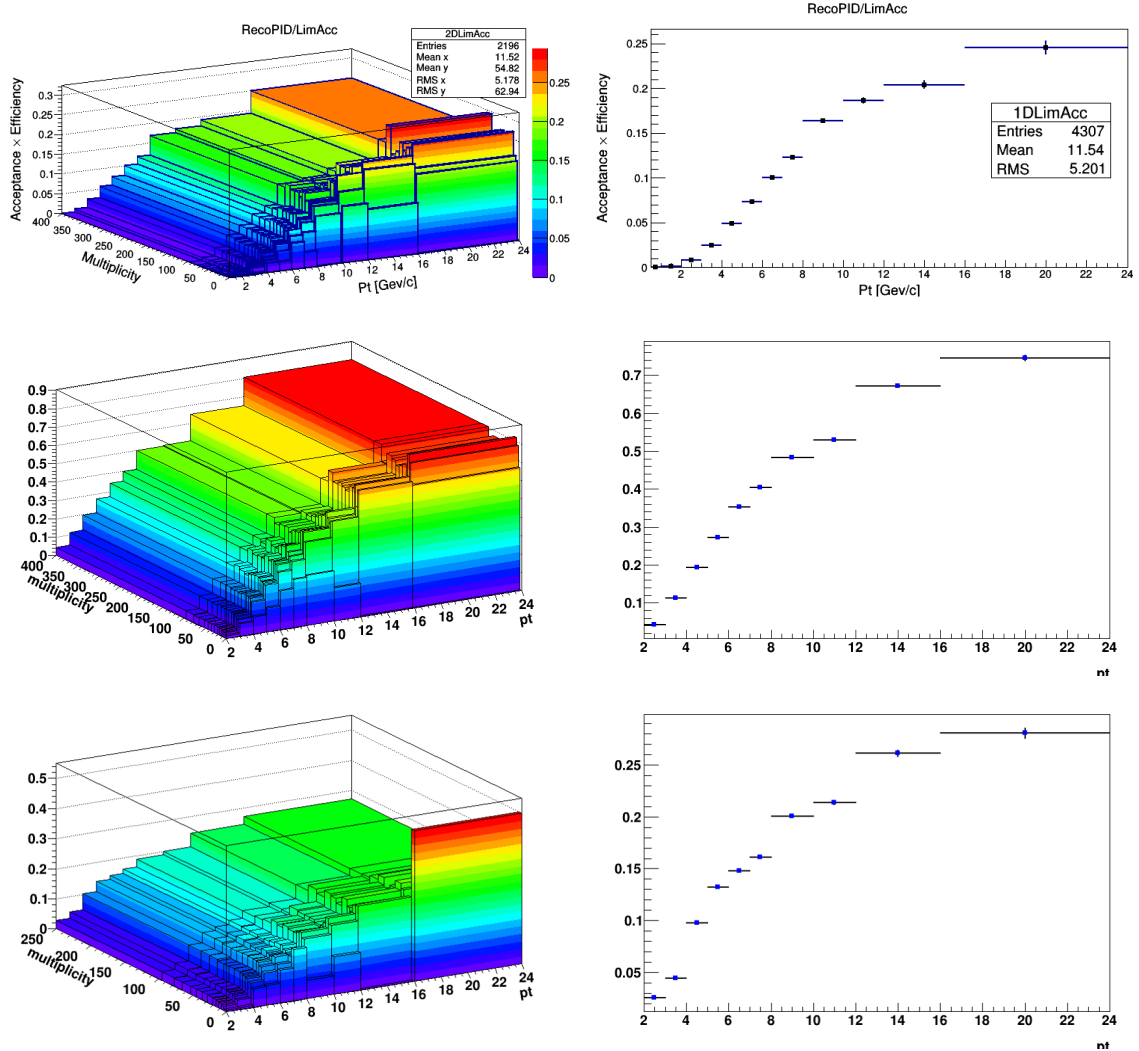


**Figure 12:** Top panel: ( $p_T$ , multiplicity) dependence (left) and  $p_T$  dependence (right) of feed-down  $D^+$  meson efficiency. Mid panel: ( $p_T$ , multiplicity) dependence (left) and  $p_T$  dependence (right) of feed-down  $D^{*+}$  meson efficiency. Bottom panel: ( $p_T$ , multiplicity) dependence (left) and  $p_T$  dependence (right) of feed-down  $D^0$  meson efficiency.

310 **3.3.3 Beauty feed-down**

311 The contribution of correlations of D meson from b-hadron decay is subtracted from the data correlation  
 312 distributions as:

$$\tilde{C}_{\text{prompt D}}(\Delta\phi) = \frac{1}{f_{\text{prompt}}} \left( \tilde{C}_{\text{inclusive}}(\Delta\phi) - (1 - f_{\text{prompt}}) \tilde{C}_{\text{feed-down}}^{\text{MC templ}}(\Delta\phi) \right). \quad (3)$$

313 In the above equation,  $\tilde{C}_{\text{inclusive}}(\Delta\phi)$  and  $\tilde{C}_{\text{prompt D}}(\Delta\phi)$  are per-trigger azimuthal correlation distributions  
 314 before and after feed-down contribution subtraction,  $f_{\text{prompt}}$  is the fraction of prompt D meson  
 315 and  $\tilde{C}_{\text{feed-down}}^{\text{MC templ}}$  is a template of the azimuthal correlation distribution for the feed-down component ob-  
 316 tained from home-made Monte Carlo simulation at generated level, using PYTHIA6 with Perugia2011  
 317 tune. In order to avoid biases related to the different event multiplicity in real and simulated events,  
 318 the correlation distribution was shifted to have its minimum coinciding with the baseline of the data  
 319 azimuthal-correlation distribution before feed-down subtraction.

320 The value of  $f_{\text{prompt}}$  (Figure 13), which depends on D-meson species and varies as a function of the  $p_T$ ,  
 321 is estimated on the basis of FONLL predictions for the production of feed-down D mesons at central  
 322 rapidity, in pp collisions at  $\sqrt{s} = 5$  TeV, and using the reconstruction efficiency of prompt and feed-  
 323 down D mesons, following the so-called  $N_b$  approach defined in [1]. Typical values ranges are about  
 324 8-10% for the  $D^0$ , about 4-7% for the  $D^+$  and about 5-8% for the  $D^{*+}$ . The procedure adopted is the  
 325 same as what done in pp: however, in p-Pb, in order to consider a possible non-zero  $v_2$ -like modulation  
 326 of the baseline, a range of  $0 < v_2 < 0.2$  values for tracks and for secondary D mesons is considered for  
 327 the systematic uncertainty evaluation (using an hypothesis of no modulation for both cases for central  
 328 values).

329 Examples of the PYTHIA templates used for the feed-down contribution subtraction are shown in Figures  
 330 14 (Figure 15 shows the same templates but for prompt D mesons).

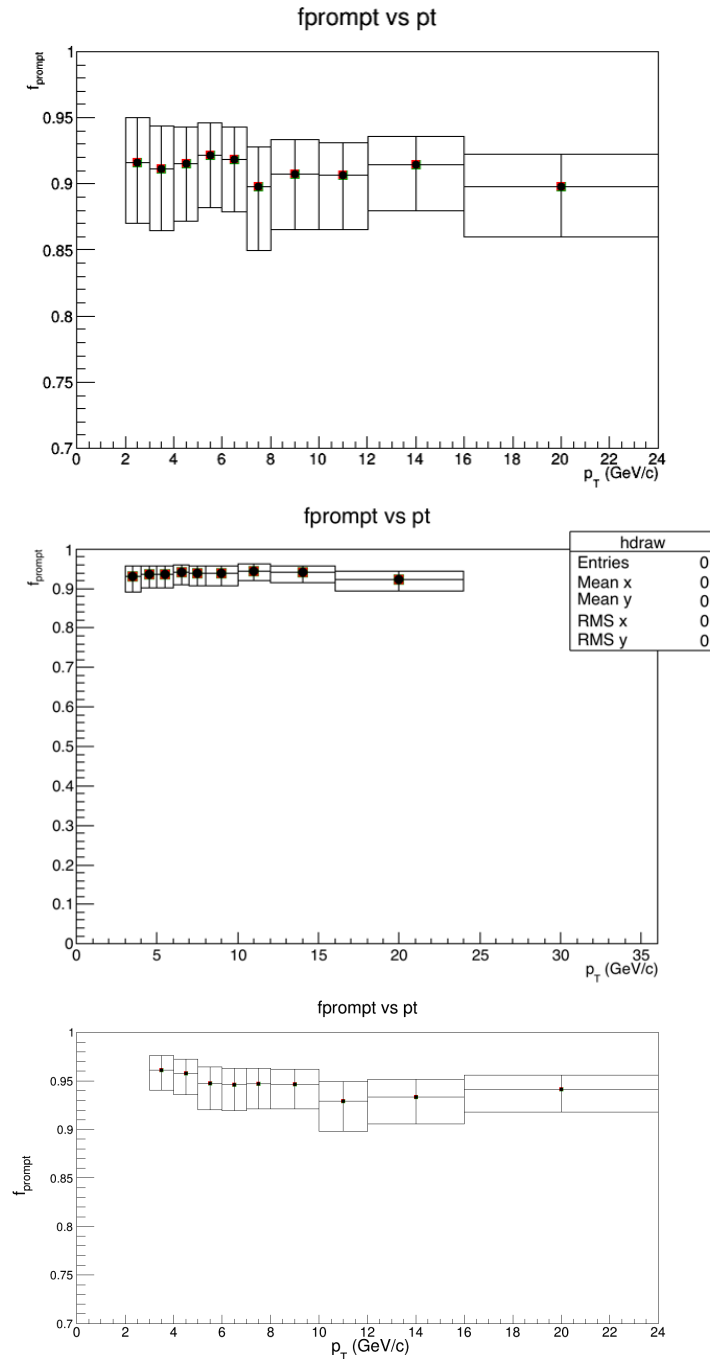


**Figure 13:**  $f_{\text{prompt}}$  as a function of the  $p_T$  for  $D^0$  (top),  $D^{*+}$  (mid) and  $D^+$  (bottom) estimated on the basis of FONLL predictions

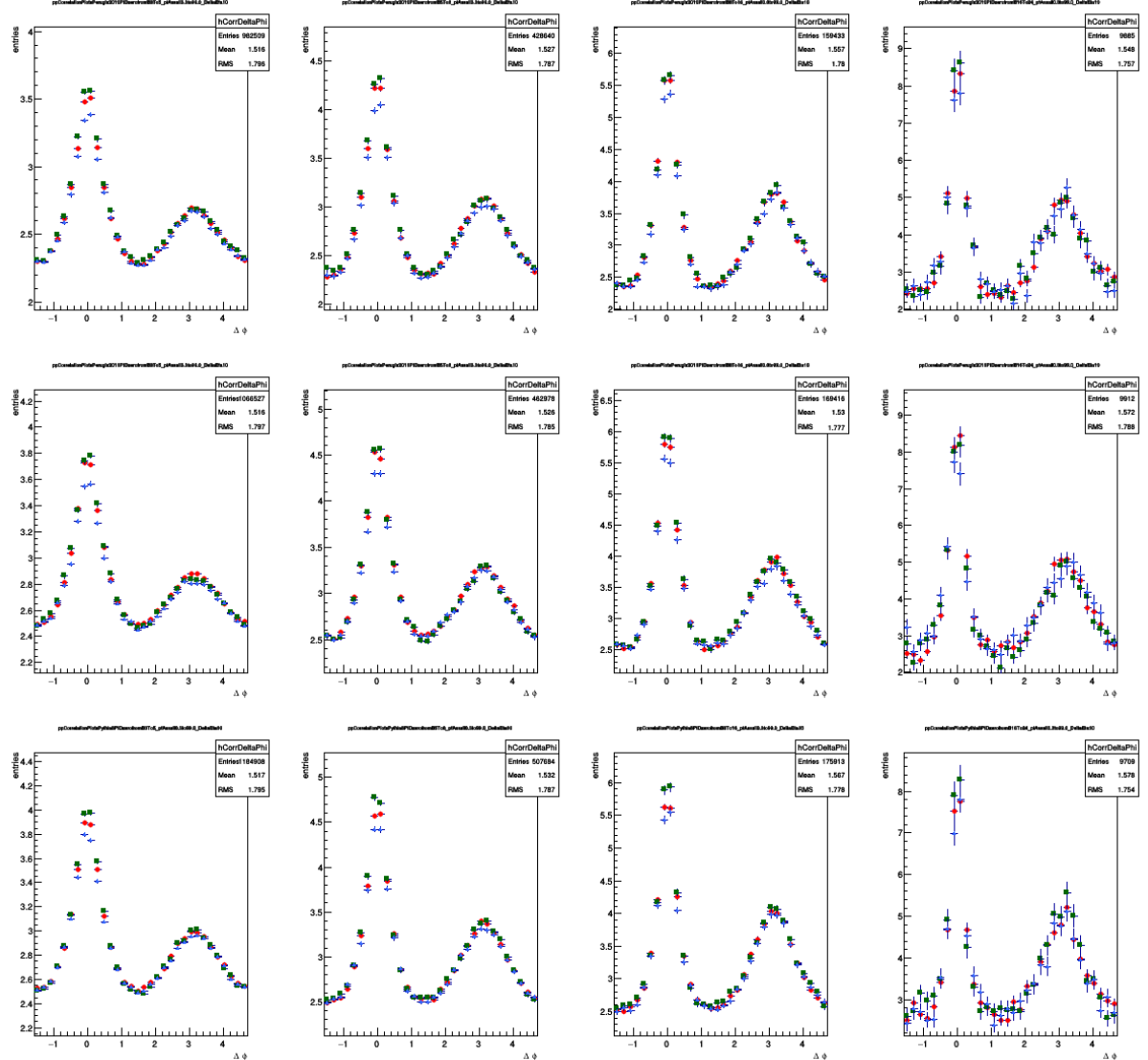


**Figure 14:** Azimuthal correlation distribution between D meson from b-hadron decay and charged particles obtained from Monte Carlo simulations based on Pythia-Perugia2010 tune (row1), Pythia-Perugia2011 tune (row2), Pythia8 tune (row3) for associated track  $p_T > 0.3$  GeV/c and D-meson pT ranges: 3-5, 5-8, 8-16, 16-24 GeV/c.  $D^0$  in blue,  $D^+$  in green,  $D^{*+}$  in red.

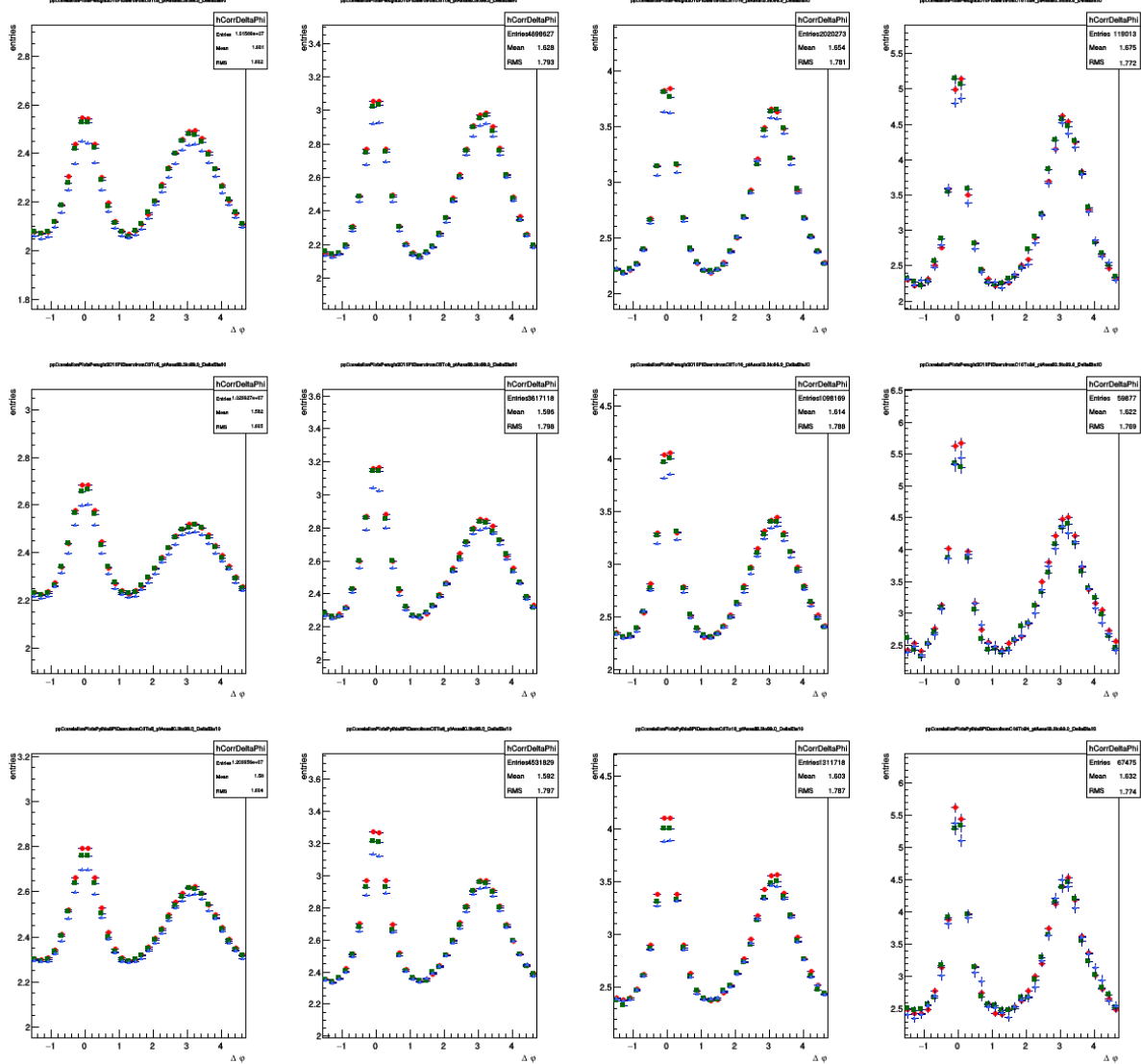


**Figure 15:** Azimuthal correlation distribution between prompt D meson and charged particles obtained from Monte Carlo simulations based on Pythia-Perugia2010 tune (row1), Pythia-Perugia2011 tune (row2), Pythia8 tune (row3) for associated track  $p_T > 0.3$  GeV/c and D-meson  $p_T$  ranges: 3-5, 5-8, 8-16, 16-24 GeV/c.  $D^0$  in blue,  $D^+$  in green,  $D^{*+}$  in red.

331 **3.3.4 Beauty feed-down**

332 The secondary tracks inside the associated track sample, due to interaction of primary track with the de-  
 333 tector material or to decays of strange hadrons, are mostly removed by the DCA cuts applied during the  
 334 cut selection phase ( $\text{DCA}(xy) > 1 \text{ cm}$ ,  $\text{DCA}(z) > 1 \text{ cm}$ ). Anyway, a small fraction of secondary tracks sur-  
 335 vives this cut, and the data correlation distributions have to be corrected for this residual contamination.  
 336 The fraction of surviving secondary tracks is evaluated via a study on the LHC17d2a\_fast\_new sample,  
 337 by counting the number of tracks accepted by the selection whose corresponding generated-level track  
 338 doesn't satisfy the `IsPhysicalPrimary()` call, and dividing this number by the total number of accepted  
 339 tracks. The outcome of the check is reported in Figure 16. As it's visible, no more than 5% secondary  
 340 tracks pass the selection. Moreover, the fraction of residual secondary tracks is flat along the  $\Delta\phi$  axis,  
 341 as shown, for exemplary  $p_T$  regions, in Figure 17, where the inhomogeneities are always below 1%. For  
 342 this reason, it is possible to directly scale the data correlation distributions by their purity fraction (i.e. 1  
 343 - secondary contamination). This is done with an associated  $p_T$  dependence, due to the increase of the  
 344 purity with the track  $p_T$ , while the purity fraction is taken flat versus the D-meson  $p_T$ . The purity values  
 345 that were chosen are the following:

- 346     –  $p_T(\text{assoc}) > 0.3 \text{ GeV}/c$ : 0.958
- 347     –  $p_T(\text{assoc}) > 1 \text{ GeV}/c$ : 0.973
- 348     –  $0.3 < p_T(\text{assoc}) < 1 \text{ GeV}/c$ : 0.953
- 349     –  $1 < p_T(\text{assoc}) < 2 \text{ GeV}/c$ : 0.969
- 350     –  $2 < p_T(\text{assoc}) < 3 \text{ GeV}/c$ : 0.982
- 351     –  $p_T(\text{assoc}) > 3 \text{ GeV}/c$ : 0.990

352 It was also verified with the same Monte Carlo study that applying the DCA selection rejects less than  
 353 0.2% primary tracks (tagged as false positives) from the associated track sample, again with a flat az-  
 354 imuthal distribution, inducing hence a fully negligible bias on the data correlation distributions. This is  
 355 shown in Figure 18. This was also verified for specific charm-origin and beauty-origin tracks, due to  
 356 their larger DCA with respect to primary tracks from light quarks. In this case, the fraction of rejected  
 357 charm and beauty tracks stays below 1% in all the kinematic ranges apart from the associated track  $p_T$   
 358 regions 0.3-1 and  $< 0.3$ , where the rejection can be as high as 2%. In these kinematic ranges, though,  
 359 the data correlation distributions are dominated by non-heavy-flavour tracks, as it was verified from the  
 360 simulations, hence the overall bias is still contained below 1%, thus negligible.

361 These studies were performed on an enriched Monte Carlo sample, which could not fully reproduce  
 362 the relative abundances of the species. Anyway, for events with a reconstructed D-meson, this bias is  
 363 expected to be minor, and only these events are used in the data analysis. In any case, the percentages  
 364 obtained from the study were found to be consistent within 1% with the outcome of the studies for the  
 365 p-Pb 2013 analysis, which reassures us on the full validity of these results.

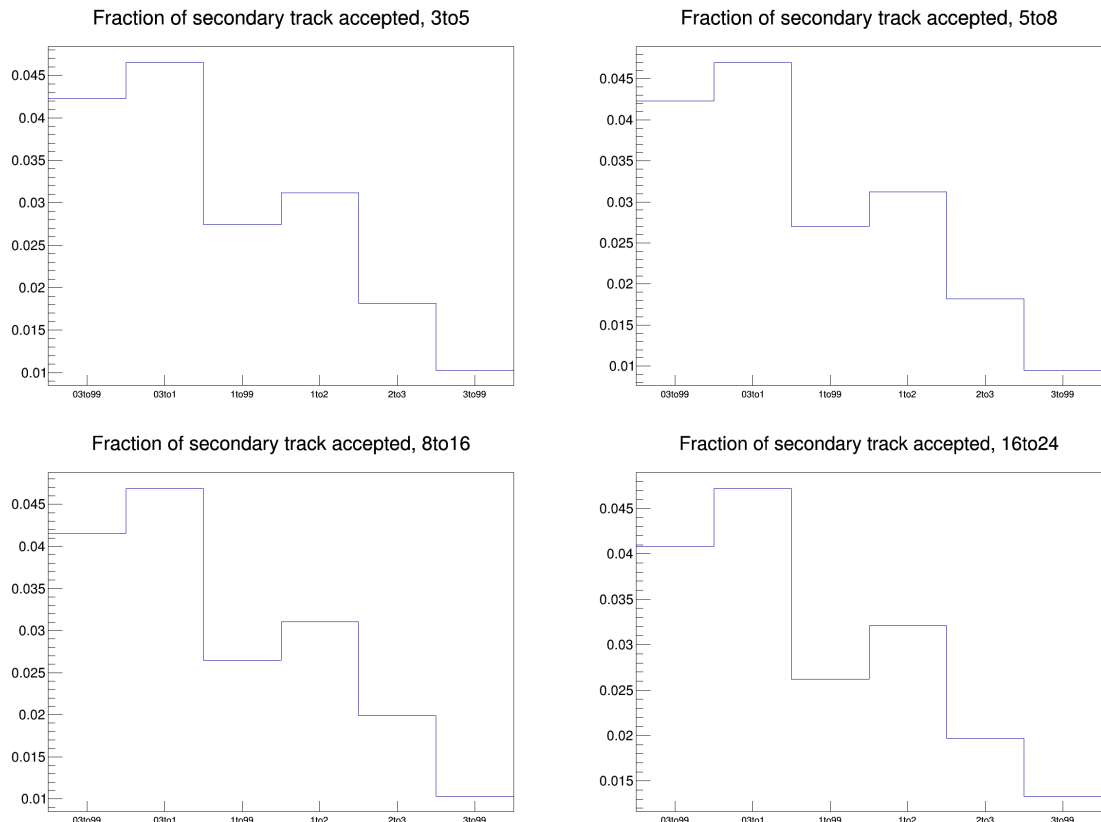


**Figure 16:** Fraction of secondary tracks over total amount of tracks which pass the DCA selection. The four panel show the fractions for the D-meson  $p_T$  ranges: 3-5, 5-8, 8-16, 16-24, respectively. Inside each panel, the associated track  $p_T$  ranges are shown on the  $x$ -axis.

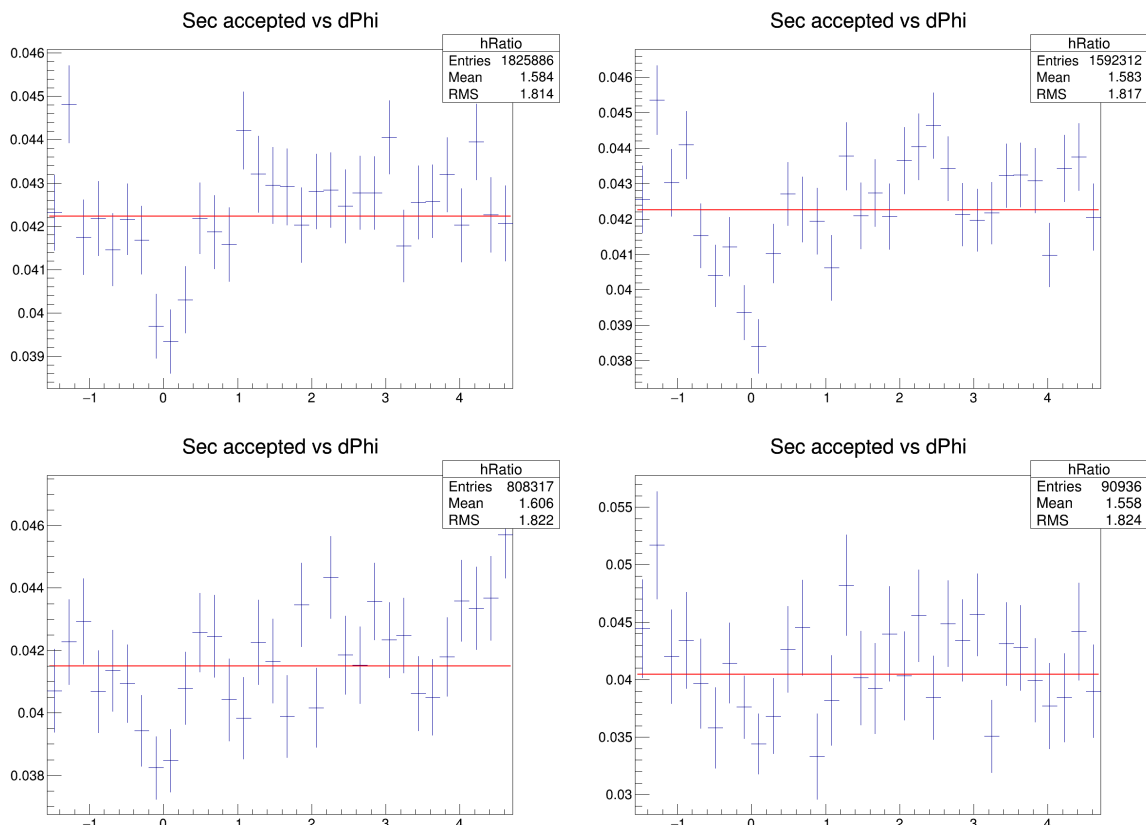


**Figure 17:**  $\Delta\phi$  dependence of the fraction of secondary tracks in the  $D^0$ - $h$  correlation distributions. The four panel show the fractions for the  $D$ -meson  $p_T$  ranges: 3-5, 5-8, 8-16, 16-24, respectively. The associated track  $p_T$  ranges is the integrated one, i.e.  $p_T > 0.3$  GeV/c.

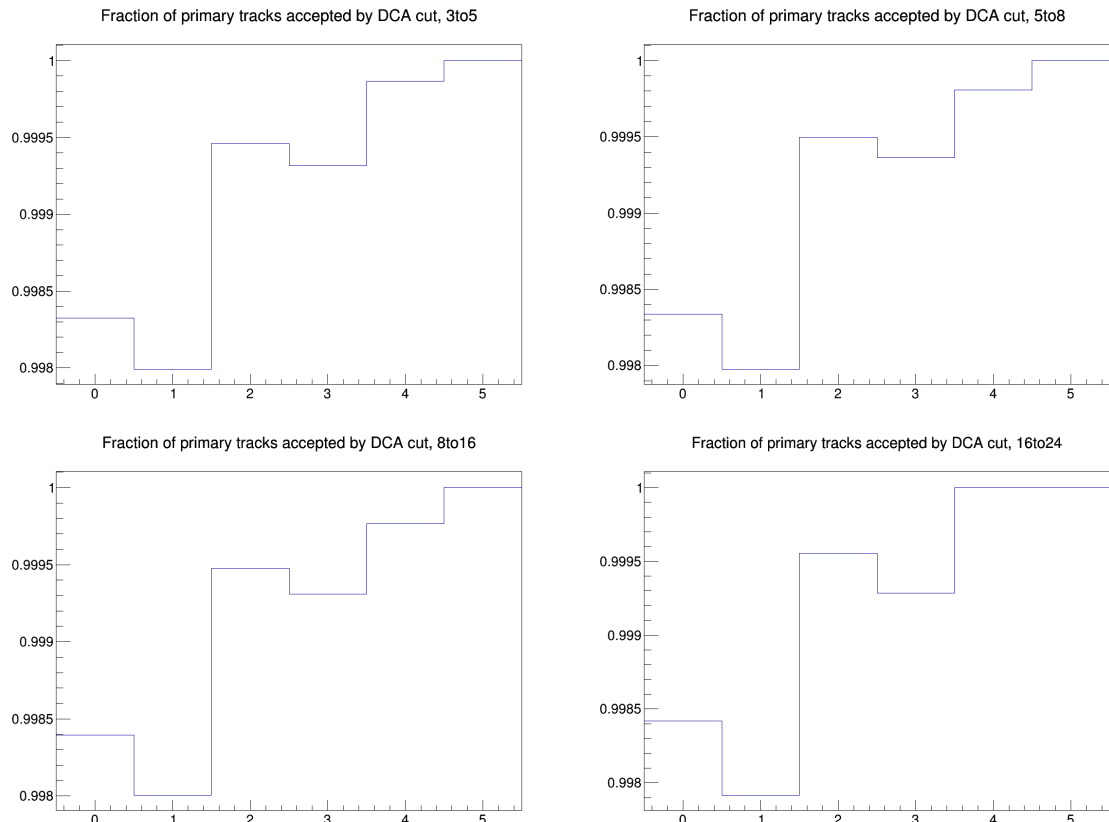


**Figure 18:** Fraction of primary tracks rejected by the DCA selection. The four panel show the fractions for the D-meson  $p_T$  ranges: 3-5, 5-8, 8-16, 16-24, respectively. Inside each panel, the associated track  $p_T$  ranges are shown on the  $x$ -axis.

<sup>366</sup> **4 Systematic uncertainties and checks of analysis consistency**

<sup>367</sup> STILL TO BE WRITTEN (MOST CHECKS ARE MISSING)

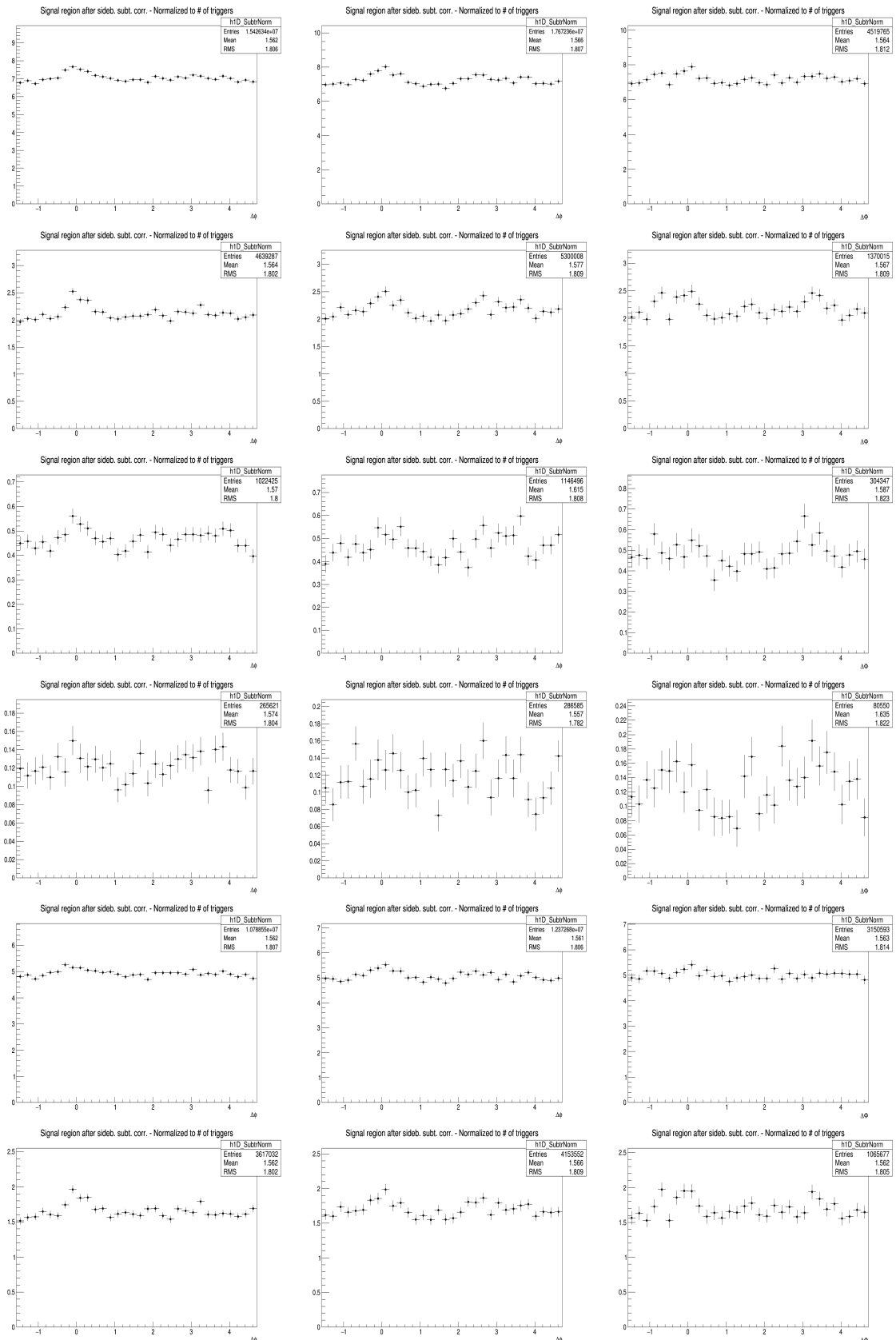
368 **5 Results**369 **5.1 Comparing the three D meson correlation distributions**

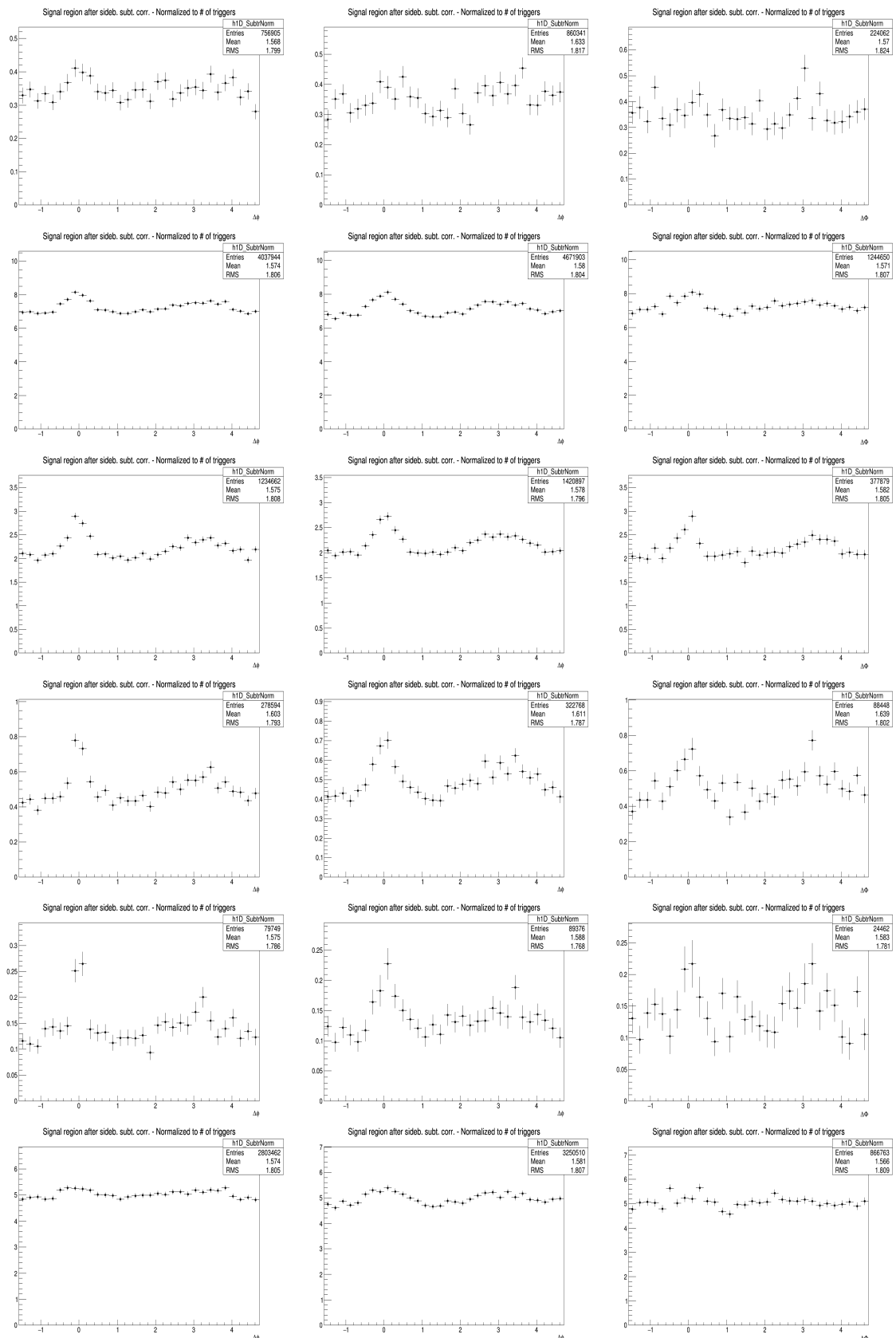
370 To check the compatibility of the three D meson analyses, Figure 19 shows the corrected and superim-  
 371 posed azimuthal correlation distributions respectively for  $D^0$ -h,  $D^{*+}$ -h and  $D^+$ -h (except for the feed-  
 372 down subtraction, on the data sample used in the analysis. Results are shown for  $3 < D p_T < 5 \text{ GeV}/c$ ,  
 373  $5 < D p_T < 8 \text{ GeV}/c$ ,  $8 < D p_T < 16 \text{ GeV}/c$  and  $16 < D p_T < 24 \text{ GeV}/c$  with associated tracks  $p_T > 0.3$ ,  
 374  $p_T > 1$ ,  $0.3 < p_T < 1 \text{ GeV}/c$ ,  $1 < p_T < 2 \text{ GeV}/c$ ,  $2 < p_T < 3 \text{ GeV}/c$  and  $p_T > 3 \text{ GeV}/c$ .

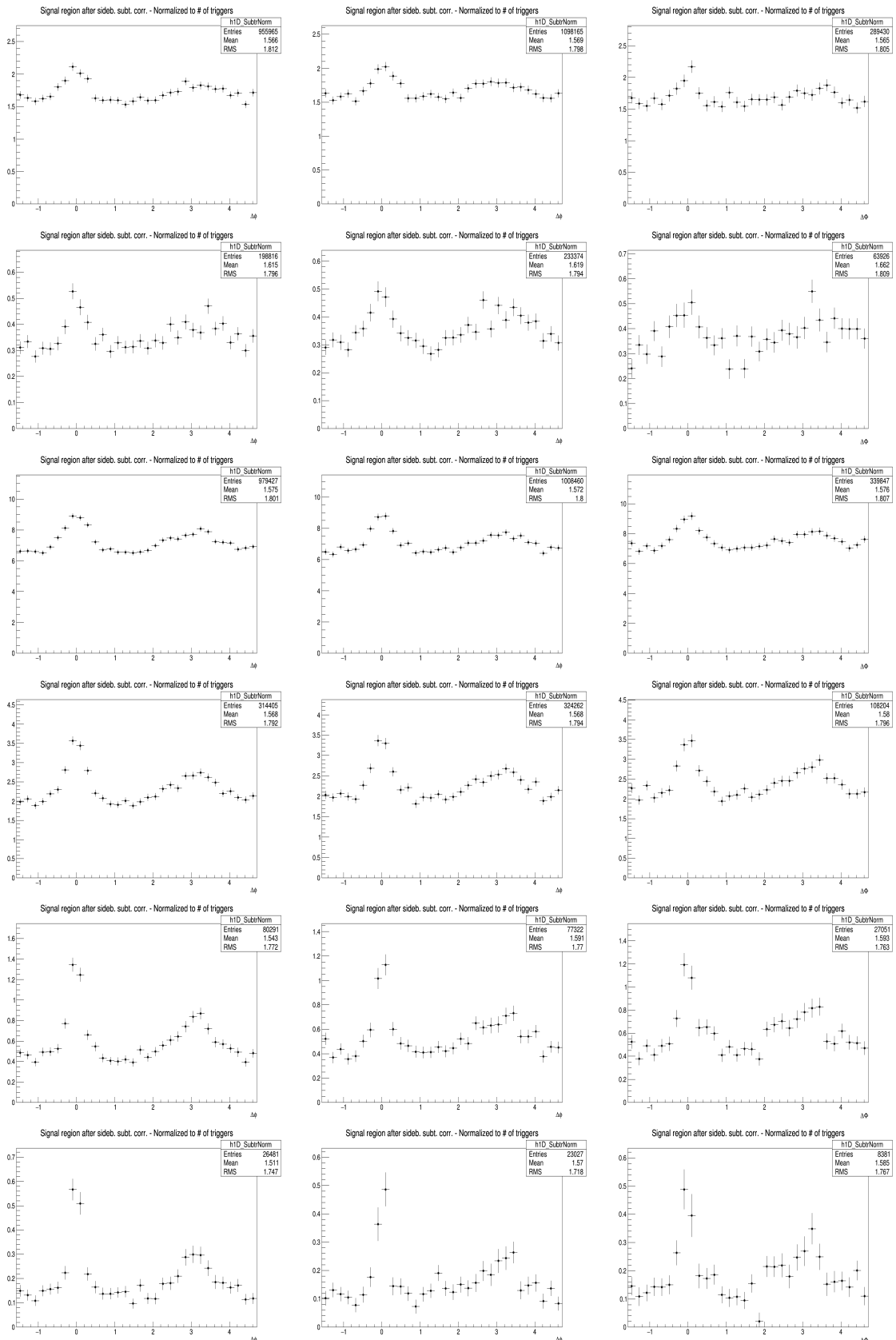
375 Figures 20, 21, 22, 23 show the superimposed correlation distributions from the single-meson analyses  
 376 (same plots as previous figure) for better visualize the agreement among the different D-meson species  
 377 results.

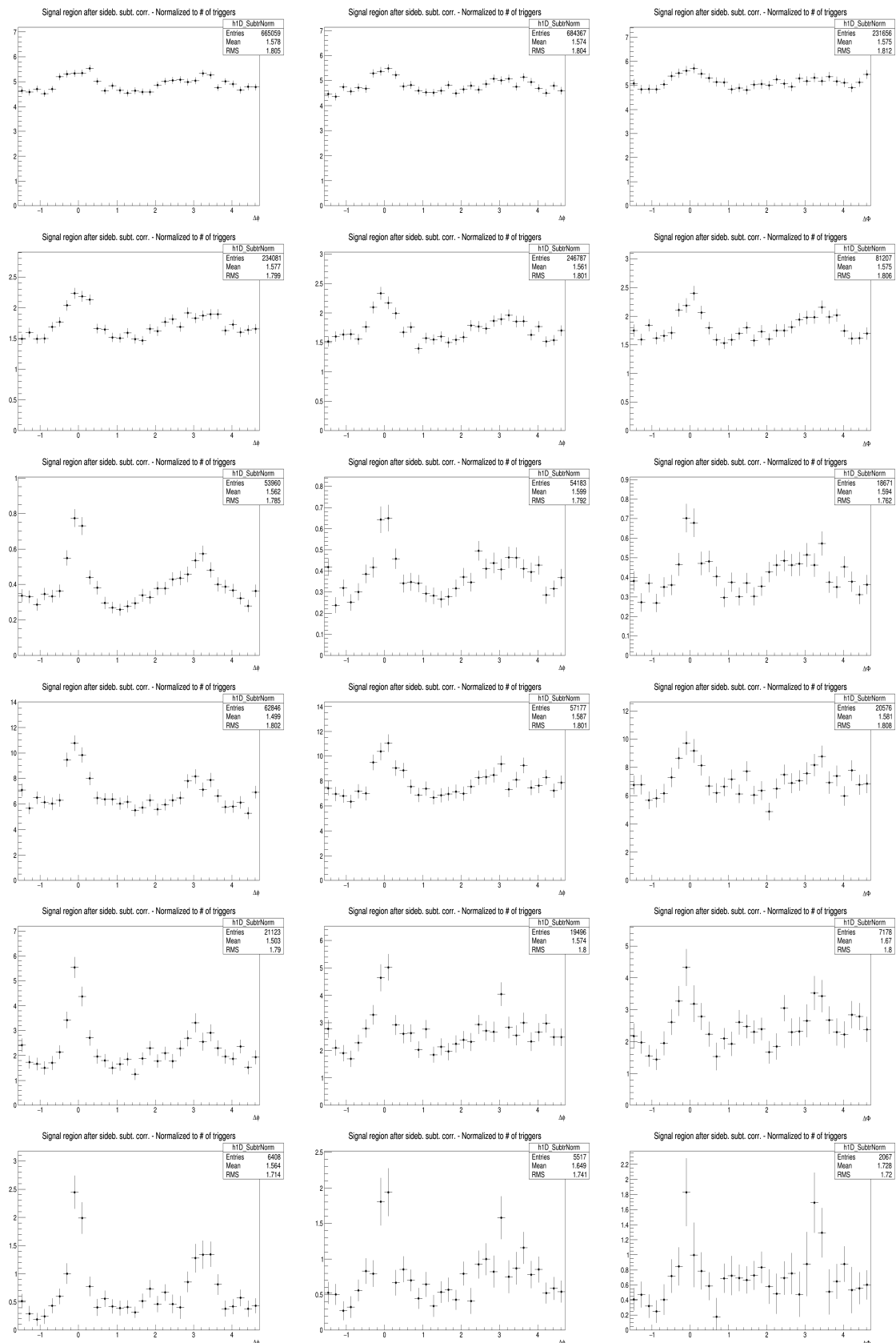
## 5.1 Comparing the three D meson correlation distributions

31









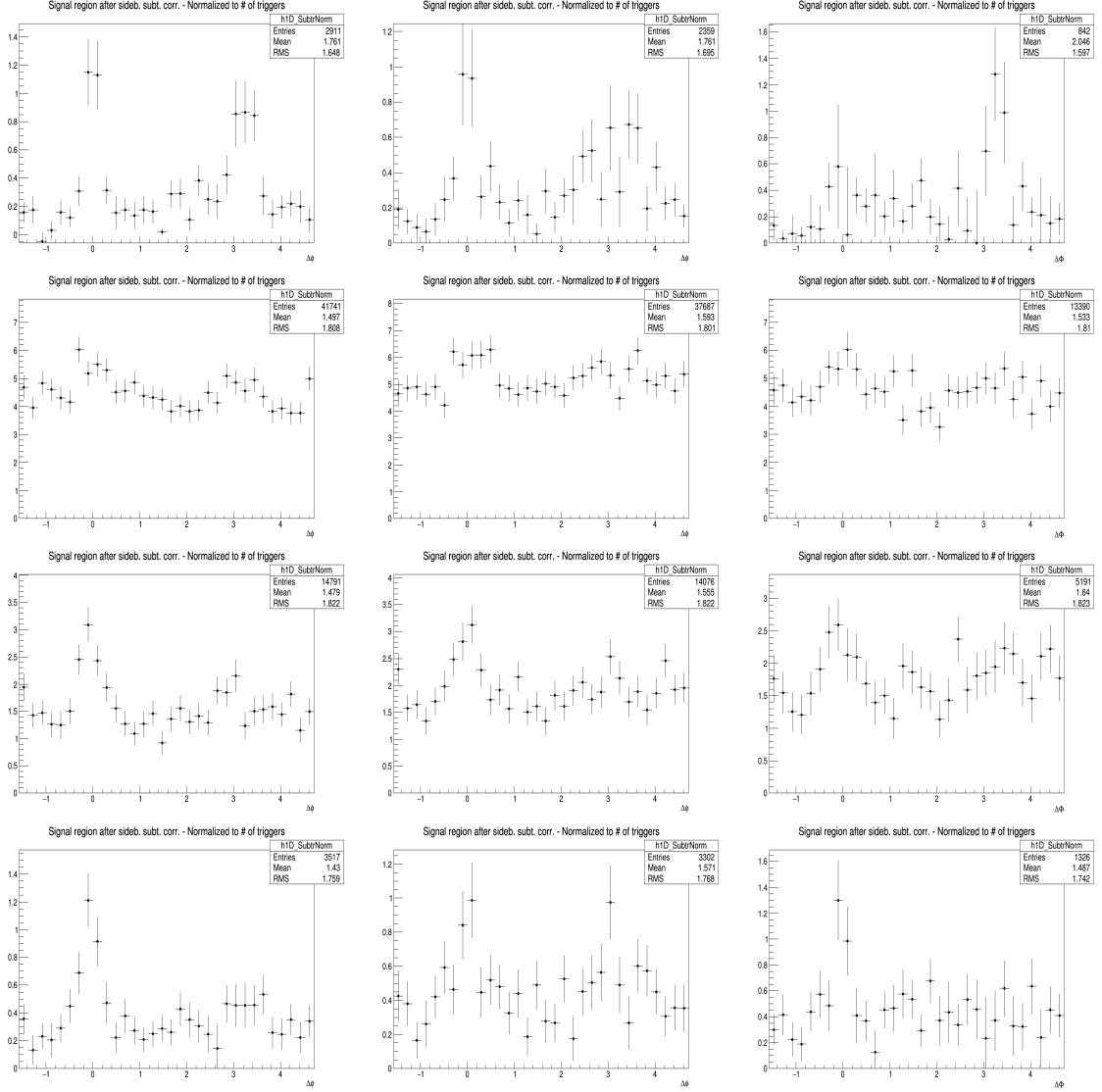


**Figure 19:** Corrected distribution of D-hadrons azimuthal correlations for the three species (apart from feed-down and purity), from analysis on the data sample, for the analyzed D-meson (**Column-Left:**  $D^0$ , **Column-Middle:**  $D^+$  and **Column-Right:**  $D^*$ ) and different associated tracks  $p_T$  ranges (**Row 1-7:**  $3 < Dp_T < 5 \text{ GeV}/c$ ,  $p_T(\text{Assoc}) > 0.3, 1.0, 2.0, 3.0, 0.3-1.0, 1.0-2.0$  and  $2.0-3.0 \text{ GeV}/c$  respectively), (**Row 8-14:**  $5 < Dp_T < 8 \text{ GeV}/c$ ,  $p_T(\text{Assoc}) > 0.3, 1.0, 2.0, 3.0, 0.3-1.0, 1.0-2.0$  and  $2.0-3.0 \text{ GeV}/c$  respectively), (**Row 15-21:**  $8 < Dp_T < 16 \text{ GeV}/c$ ,  $p_T(\text{Assoc}) > 0.3, 1.0, 2.0, 3.0, 0.3-1.0, 1.0-2.0$  and  $2.0-3.0 \text{ GeV}/c$  respectively) and (**Row 22-28:**  $16 < Dp_T < 24 \text{ GeV}/c$ ,  $p_T(\text{Assoc}) > 0.3, 1.0, 2.0, 3.0, 0.3-1.0, 1.0-2.0$  and  $2.0-3.0 \text{ GeV}/c$  respectively)

378 An agreement of the distributions from the three mesons within the uncertainties is found in all the  
 379 kinematic ranges.

380 Despite being evaluated in the full  $2\pi$  range, the range of final results was then reduced to  $[0, \pi]$  radians,  
 381 reflecting the points outside that range over the value of 0. This allowed to reduce the impact of statistical  
 382 fluctuations on the data points (supposing equal statistics for a pair of symmetric bins, after the reflection  
 383 the relative statistical uncertainty for the resulting bin is reduced by a factor  $1/\sqrt{2}$ ).

### 384 5.2 Average of $D^0$ , $D^+$ and $D^{*+}$ results

385 Given the compatibility within the uncertainties among the  $D^0$ ,  $D^+$  and  $D^{*+}$  azimuthal correlations, and  
 386 since no large differences are visible in the correlation distributions observed in Monte Carlo simulations  
 387 based on Pythia with Perugia0, 2010 and 2011 tunes<sup>1</sup>, it was possible to perform a weighted average  
 388 (eq. 4) of the azimuthal correlation distributions of  $D^0$ ,  $D^+$  and  $D^{*+}$ , in order to reduce the overall  
 389 uncertainties. Although some correlation between the mesons could be present (about the 30% of the  
 390  $D^0$ , and also part of the  $D^+$ , come from  $D^{*+}$  decays), the three selected D-meson samples can be treated  
 391 as uncorrelated. The inverse of the sum in quadrature of the statistical uncertainty, of the S and B  
 392 extraction uncertainty, and of the background shape systematic uncertainty was used as weight.

$$\left\langle \frac{1}{N_D} \frac{dN_{\text{assoc}}}{dp_T} \right\rangle_{D\text{mesons}} = \frac{\sum_{i=\text{meson}} w_i \frac{1}{N_D} \frac{dN_i^{\text{assoc}}}{d\Delta\phi}}{\sum_{i=\text{meson}} w_i}, w_i = \frac{1}{\sigma_{i,\text{stat}}^2 + \sigma_{i,\text{uncorr.syst}}^2} \quad (4)$$

393 The statistical uncertainty and the uncertainties on S and B extraction and on background shape (those  
 394 used for the weights) on the average were then recalculated using the following formula:

$$\sigma^2 = \frac{1}{n_D} \frac{\sum_{i=\text{meson}} w_i \sigma_i^2}{\sum_{i=\text{meson}} w_i} \quad (5)$$

395 where  $n_D$  is the number of mesons considered in the average. It can be observed that for  $\sigma_i^2 = 1/w_i$  the  
 396 formula coincides with the standard one giving the uncertainty on a weighted average. The contribution  
 397 to the average systematic uncertainty for those uncertainty sources not included in the weight definition,  
 398 was evaluated via error propagation on the formula of the weighted average (4), resulting in equation  
 399 (6) and (7) for sources considered uncorrelated and correlated among the mesons. In particular, the  
 400 uncertainties on the associated track reconstruction efficiency, on the contamination from secondary, on  
 401 the feed-down subtraction, and that resulting from the Monte Carlo closure test were considered fully  
 402 correlated among the mesons, while those deriving from the yield extraction (included in the weight  
 403 definition) and on the D meson reconstruction and selection efficiency were treated as uncorrelated.

$$\sigma^2 = \frac{\sum_{i=\text{meson}} w_i^2 \sigma_i^2}{(\sum_{i=\text{meson}} w_i)^2} \quad (6)$$

$$\sigma = \frac{\sum_{i=\text{meson}} w_i \sigma_i}{\sum_{i=\text{meson}} w_i} \quad (7)$$

404 Figure 24 shows the averages of the azimuthal correlation distributions of  $D^0$ ,  $D^+$  and  $D^{*+}$  and charged  
 405 particles with  $p_T > 0.3 \text{ GeV}/c$ ,  $0.3 < p_T < 1 \text{ GeV}/c$ ,  $p_T > 1 \text{ GeV}/c$ ,  $1 < p_T < 2 \text{ GeV}/c$ ,  $2 < p_T <$   
 406  $3 \text{ GeV}/c$ ,  $p_T < 3 \text{ GeV}/c$  in the D meson  $p_T$  ranges  $3 < p_T < 5 \text{ GeV}/c$ ,  $5 < p_T < 8 \text{ GeV}/c$ ,  $8 < p_T <$   
 407  $16 \text{ GeV}/c$  and  $16 < p_T < 24 \text{ GeV}/c$ . As expected, a rising trend of the height of the near-side peak with  
 408 increasing D-meson  $p_T$  is observed, together with a decrease of the baseline level with increasing  $p_T$  of  
 409 the associated tracks.

---

<sup>1</sup>A slight near side hierarchy is present among the three meson results, with  $D^{*+}$  meson having a lower peak amplitude than  $D^0$  and  $D^+$ . It was verified that this is induced by the presence of  $D^0$  and  $D^+$  mesons coming from  $D^{*+}$ , the latter having on average a larger  $p_T$  and coming, hence, on average, from a larger  $p_T$  quark parton, which fragments in slightly more tracks in the near-side.

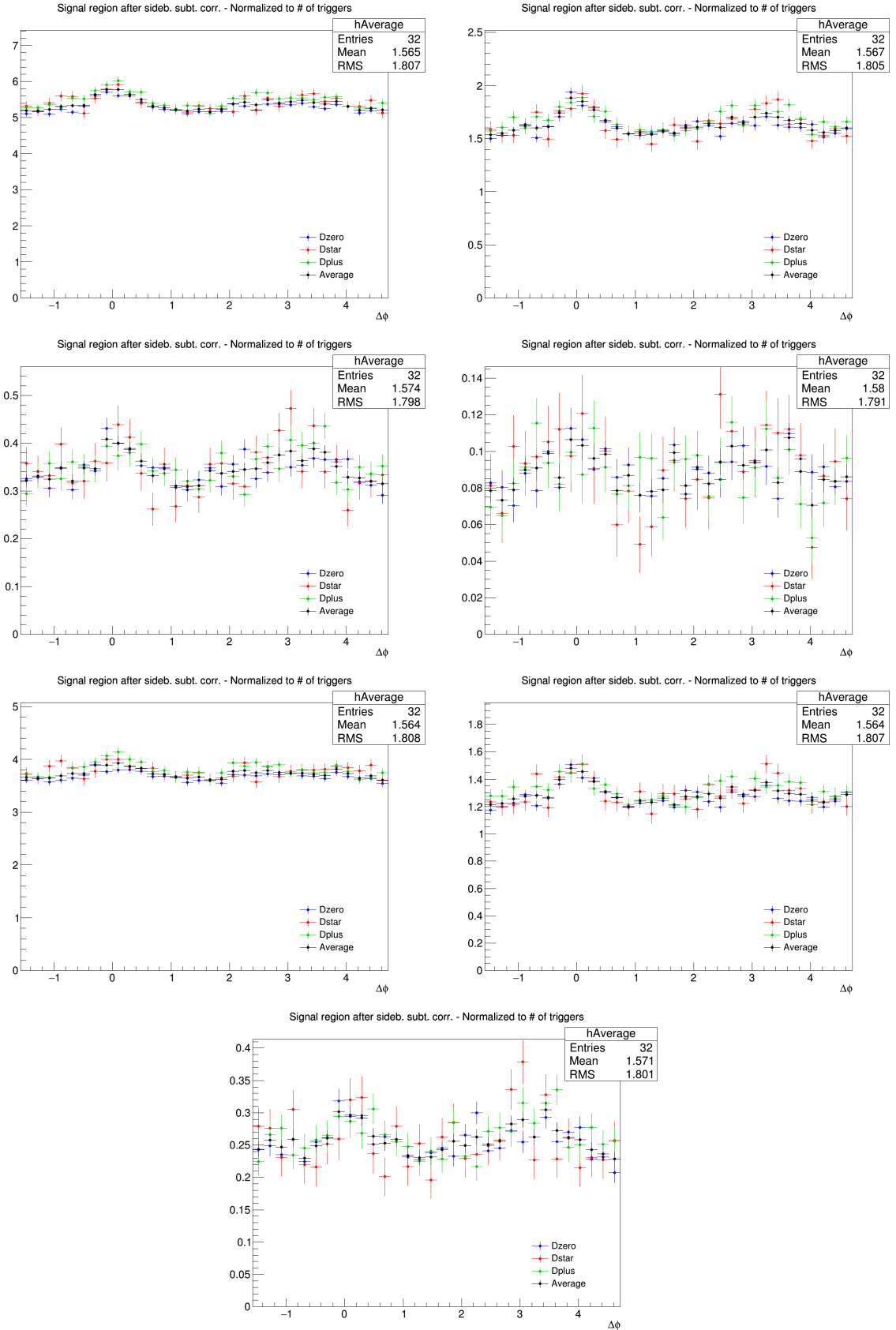


**Figure 20:** Superimposition of the corrected distribution of D-hadrons azimuthal correlations for the three species (apart from feed-down and purity), from analysis on the data sample, for the analyzed D-meson and different associated track  $p_T$  ranges, and D-meson  $p_T$  3-5 GeV/c. **Panels from 1 to 7 of each page:**  $p_T(\text{Assoc}) > 0.3, > 1.0, > 2.0, > 3.0, 0.3-1.0, 1.0-2.0$  and  $2.0-3.0 \text{ GeV}/c$

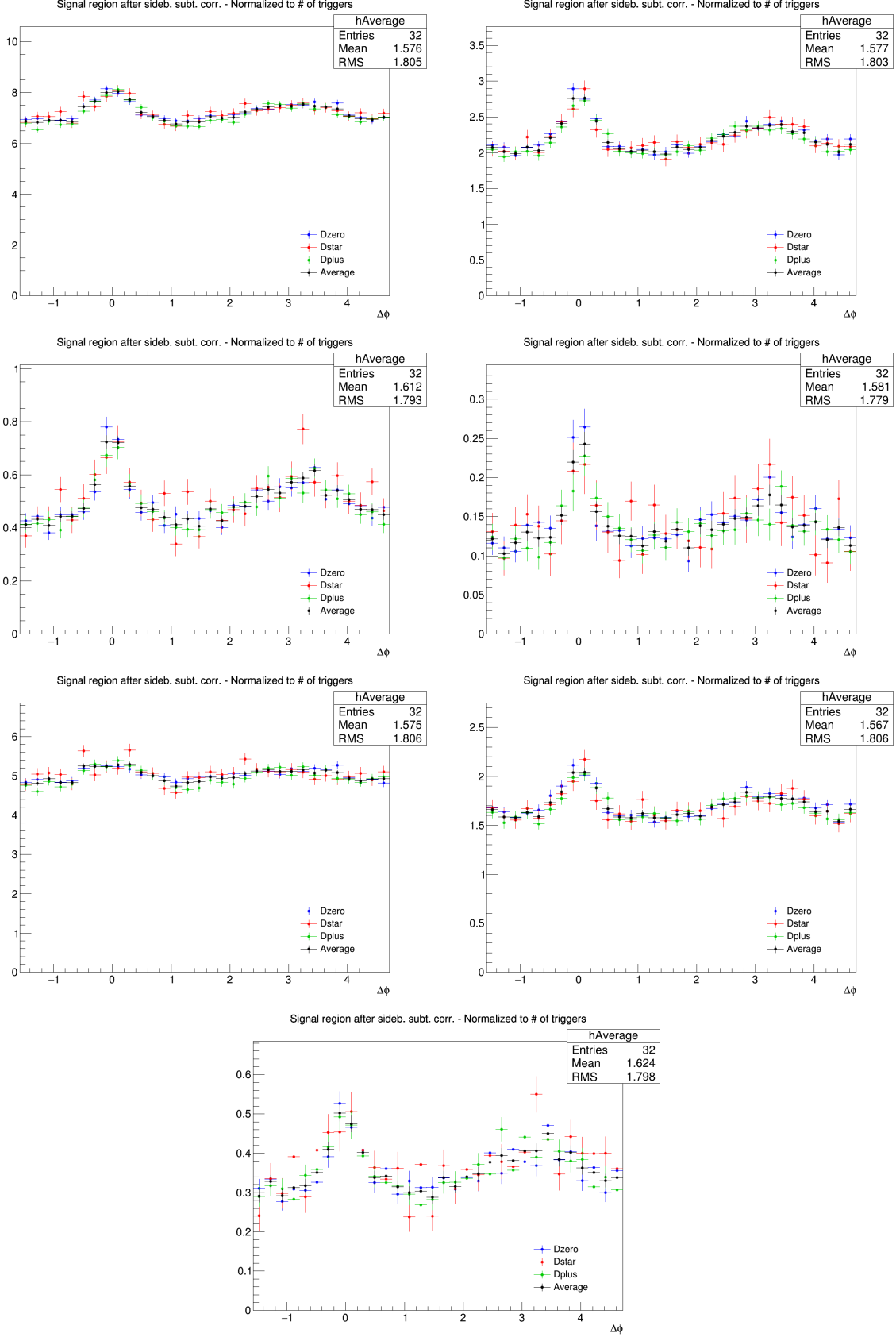


**Figure 21:** Superimposition of the corrected distribution of D-hadrons azimuthal correlations for the three species (apart from feed-down and purity), from analysis on the data sample, for the analyzed D-meson and different associated track  $p_T$  ranges, and D-meson  $p_T$  5-8 GeV/c. **Panels from 1 to 7 of each page:**  $p_T(\text{Assoc}) > 0.3, > 1.0, > 2.0, > 3.0, 0.3-1.0, 1.0-2.0$  and  $2.0-3.0$  GeV/c

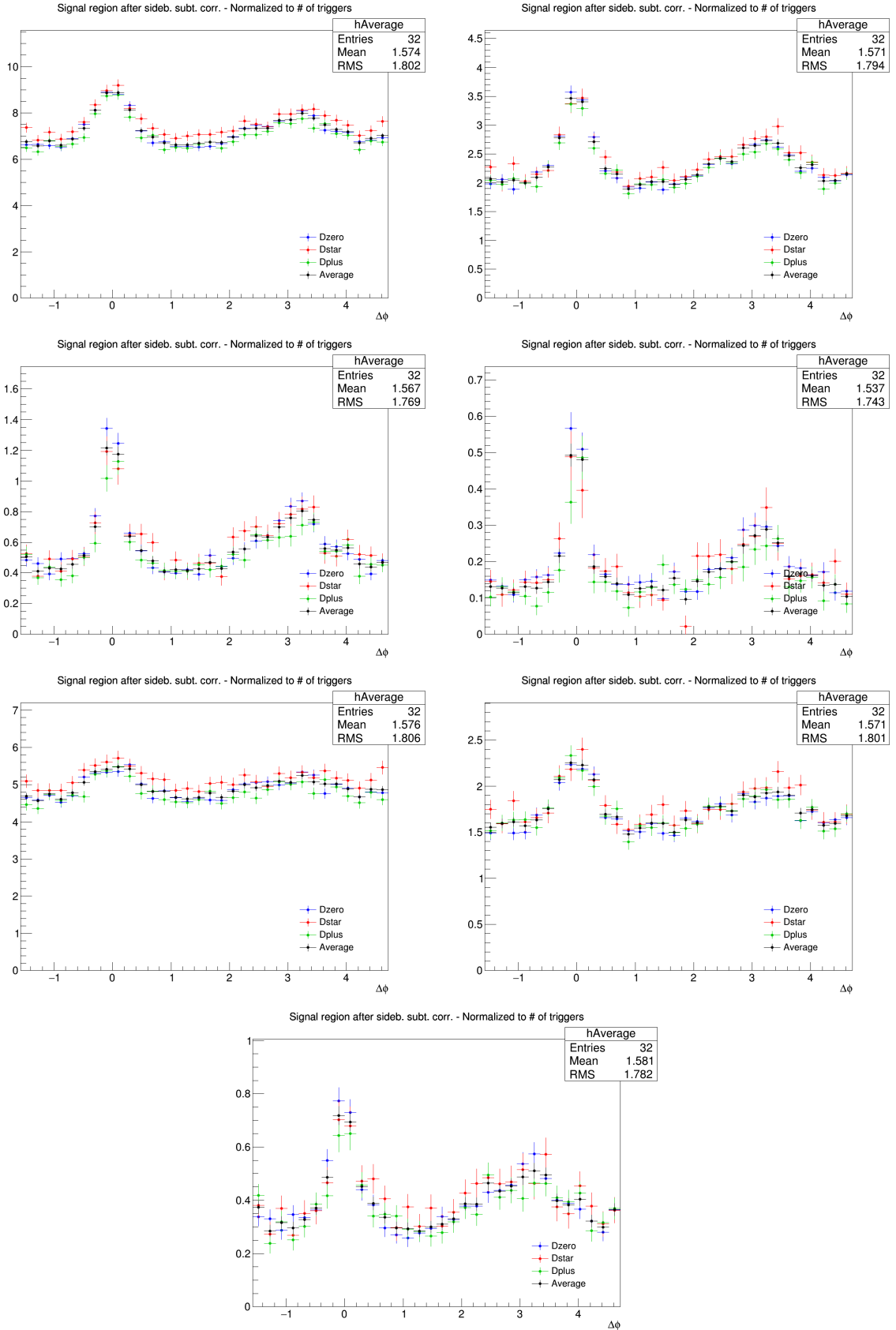


**Figure 22:** Superimposition of the corrected distribution of D-hadrons azimuthal correlations for the three species (apart from feed-down and purity), from analysis on the data sample, for the analyzed D-meson and different associated track  $p_T$  ranges, and D-meson  $p_T$  8-16 GeV/c. **Panels from 1 to 7 of each page:**  $p_T$  (*Assoc*) > 0.3, >1.0, >2.0, >3.0, 0.3-1.0, 1.0-2.0 and 2.0-3.0 GeV/c

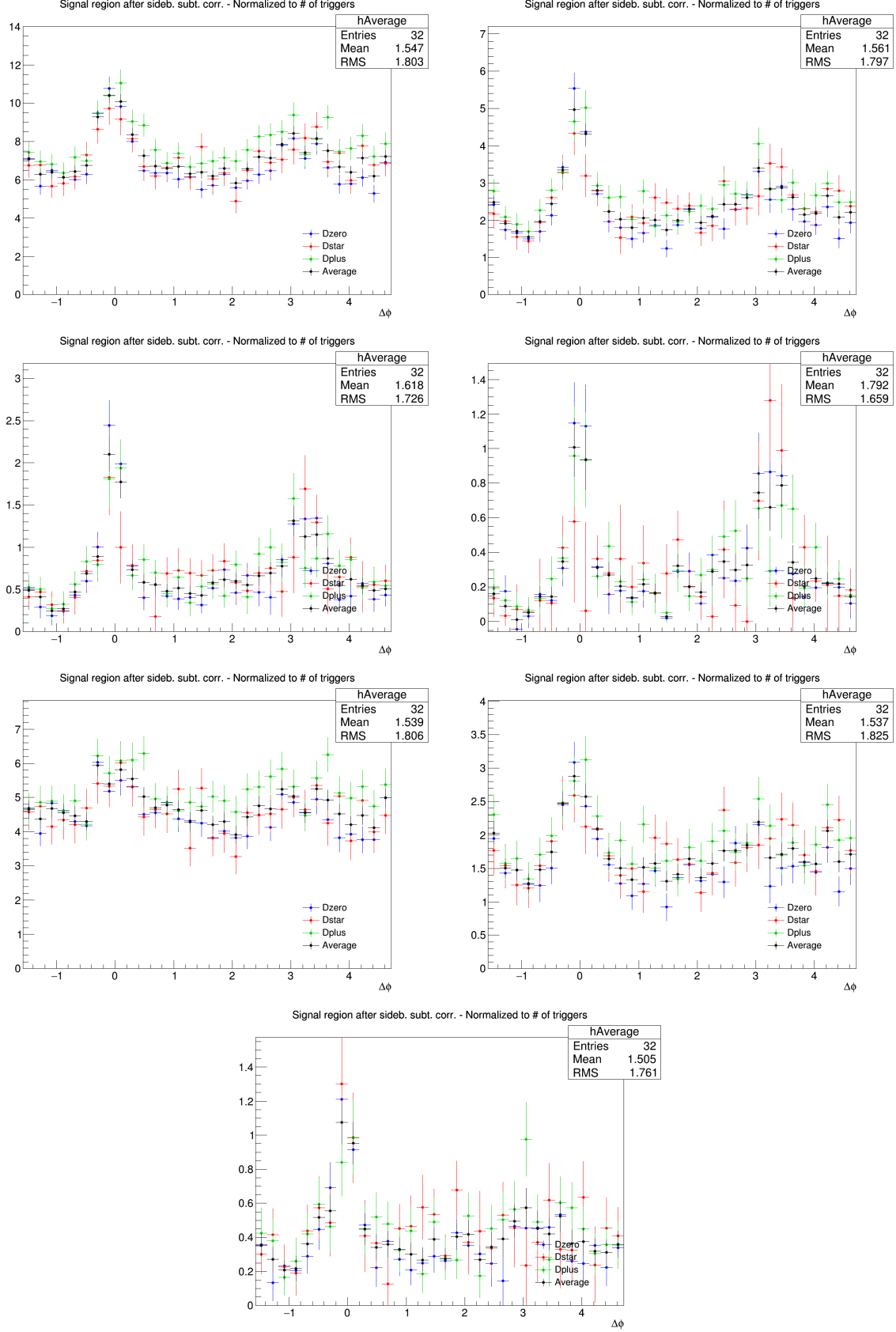
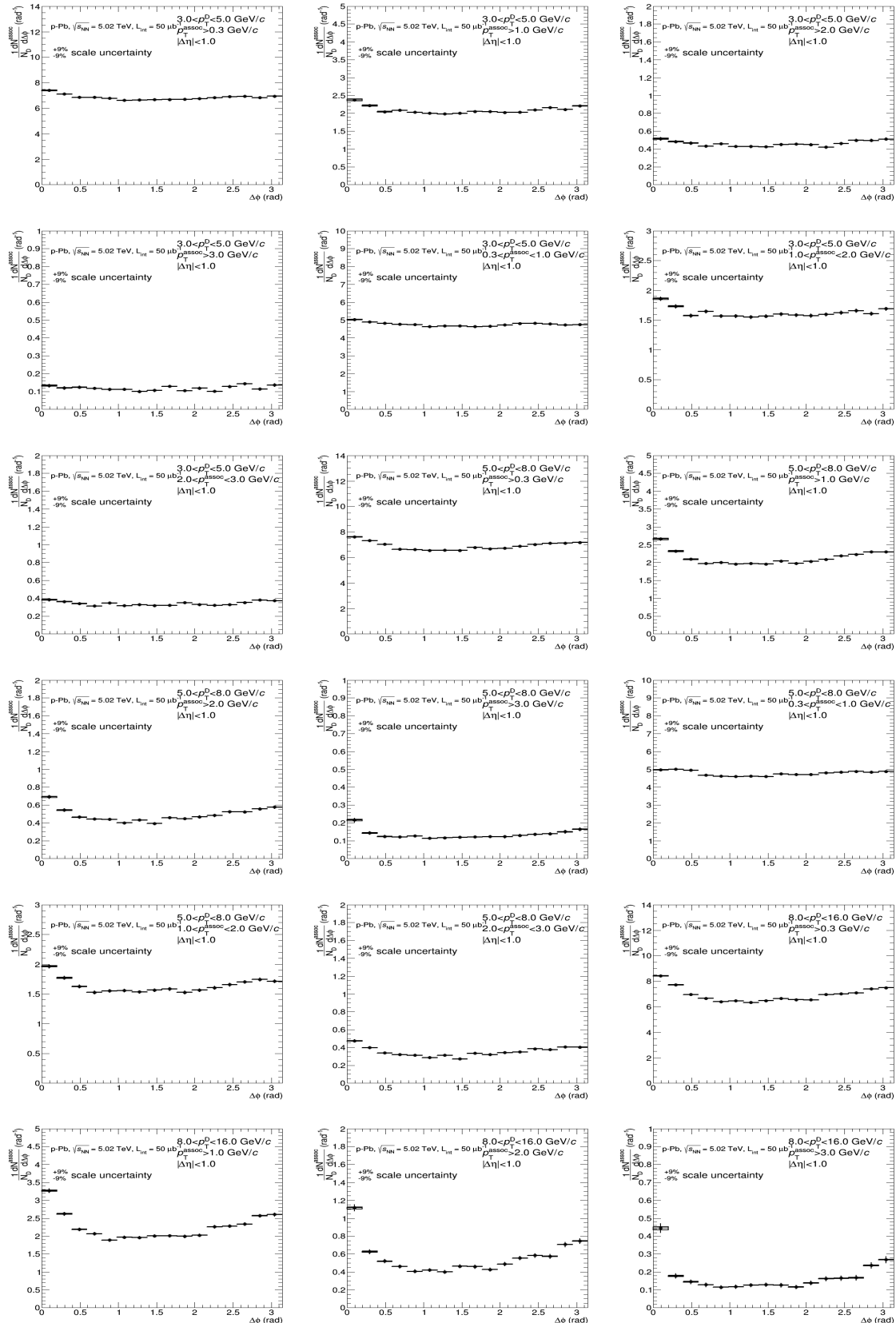


**Figure 23:** Superimposition of the corrected distribution of D-hadrons azimuthal correlations for the three species (apart from feed-down and purity), from analysis on the data sample, for the analyzed D-meson and different associated track  $p_T$  ranges, and D-meson  $p_T$  16-24 GeV/c. **Panels from 1 to 7 of each page:**  $p_T(\text{Assoc}) > 0.3, > 1.0, > 2.0, > 3.0, 0.3-1.0, 1.0-2.0$  and  $2.0-3.0 \text{ GeV}/c$

## 5.2 Average of $D^0$ , $D^+$ and $D^{*+}$ results

41



410 The usage of weighted average requires, as an underlying assumption, identical results expected for  
411 different species (or, at least, compatible within the uncertainties).

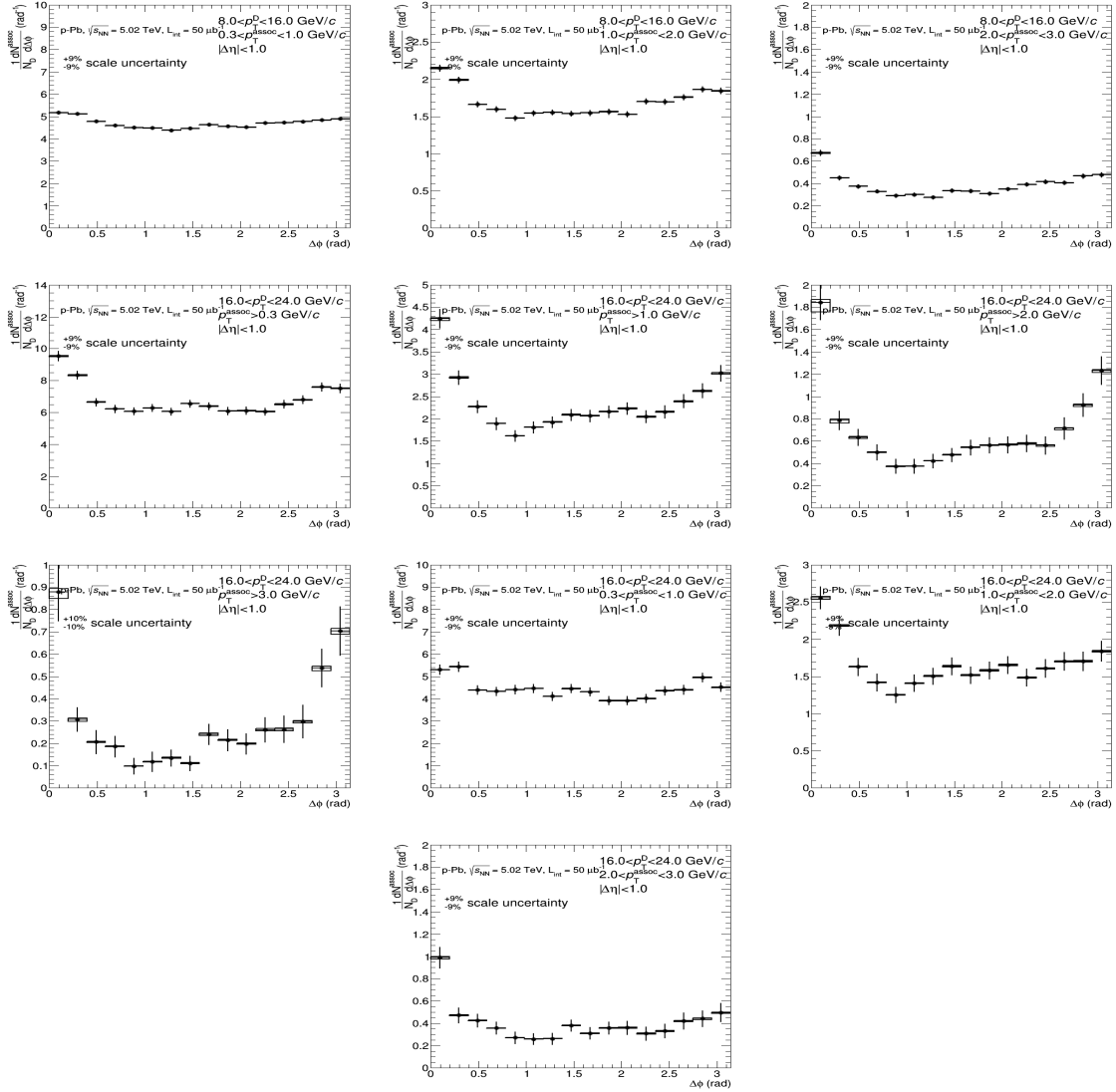


**Figure 24:** Average of  $D^0$ ,  $D^+$  and  $D^{*+}$  azimuthal correlation distributions, in the  $D$  meson  $p_T$  ranges  $5 < p_T < 8$   $\text{GeV}/c$  and  $8 < p_T < 16$   $\text{GeV}/c$ , with associated tracks with  $p_T > 0.3$   $\text{GeV}/c$ ,  $p_T > 1$   $\text{GeV}/c$  and  $0.3 < p_T < 1$   $\text{GeV}/c$ .

412 **5.3 Fit observable  $p_T$  trends and uncertainties**

413 In order to extract quantitative and physical information from the data correlation patterns, the averaged  
 414 D-h correlation distributions are fitted with two Gaussian functions (with means fixed at  $\Delta\phi=0$  and  $\Delta\phi=\pi$   
 415 values), plus a constant term (baseline). A periodicity condition is also applied to the fit function to obtain  
 416 the same value at the bounds of  $2\pi$  range. The expression of the fit expression is reported below (equation  
 417 8):

$$f(\Delta\phi) = c + \frac{Y_{NS}}{\sqrt{2\pi}\sigma_{NS}} e^{-\frac{(\Delta\phi-\mu_{NS})^2}{2\sigma_{NS}^2}} + \frac{Y_{AS}}{\sqrt{2\pi}\sigma_{AS}} e^{-\frac{(\Delta\phi-\mu_{AS})^2}{2\sigma_{AS}^2}} \quad (8)$$

418 where baseline is calculated as the weighted average of the points lying in the so-called "transverse  
 419 region", i.e. the interval  $\frac{\pi}{4} < |\Delta\phi| < \frac{\pi}{2}$ .

420 An example of the results from the fit is shown in Figure 25

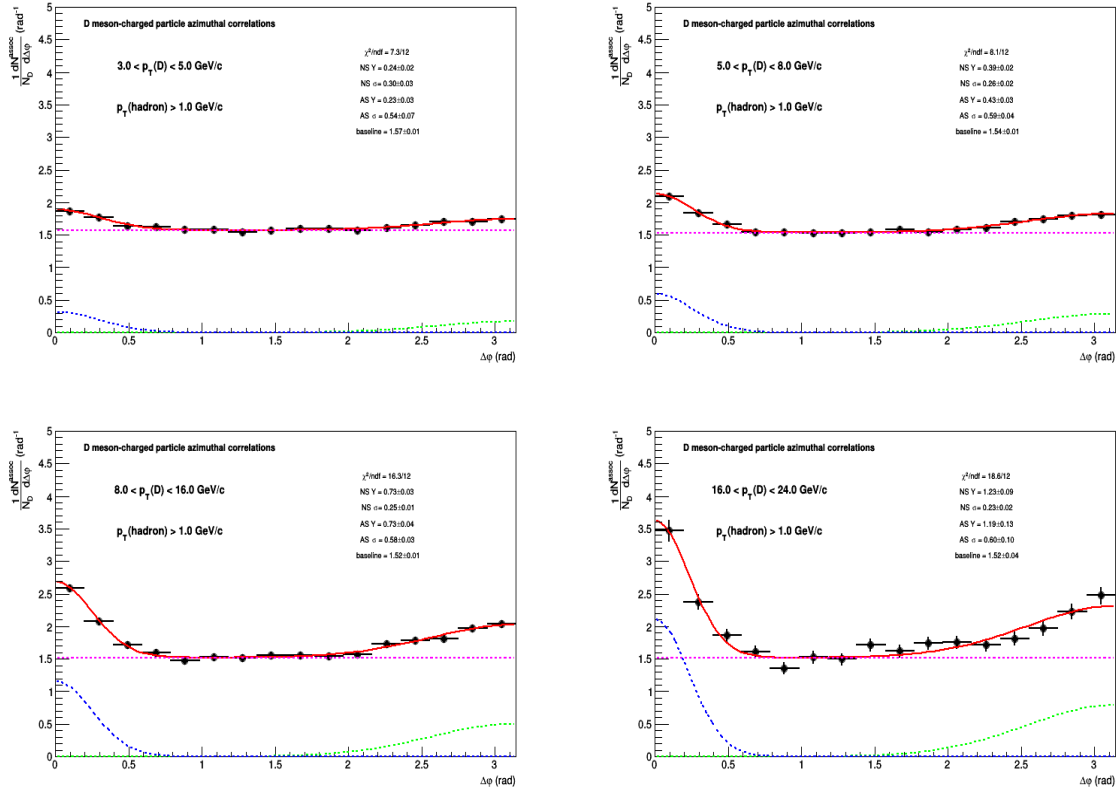


Figure 25: Example of fit to azimuthal correlation distributions and baseline estimation.

421 From the fit outcome is it possible to retrieve the near-side and away-side yield and widths (integral and  
 422 sigma of the Gaussian functions, respectively), as well as the baseline height. The near-side observables  
 423 give information on the multiplicity and angular spread of the tracks from the fragmentation of the charm  
 424 jet which gave birth to the D-meson trigger, while at first order the away-side observables are related to  
 425 the hadronization of the charm parton produced in the opposite direction (though the presence of NLO  
 426 processes for charm production breaks the full validity of this assumption). The baseline value is a rough  
 427 indicator of the underlying event multiplicity, though below the baseline level also charm and beauty-  
 428 related pairs are contained (especially in cases of NLO production for the heavy quarks).

429 The evaluation of the systematic uncertainties on the observables obtained from the fits is performed as

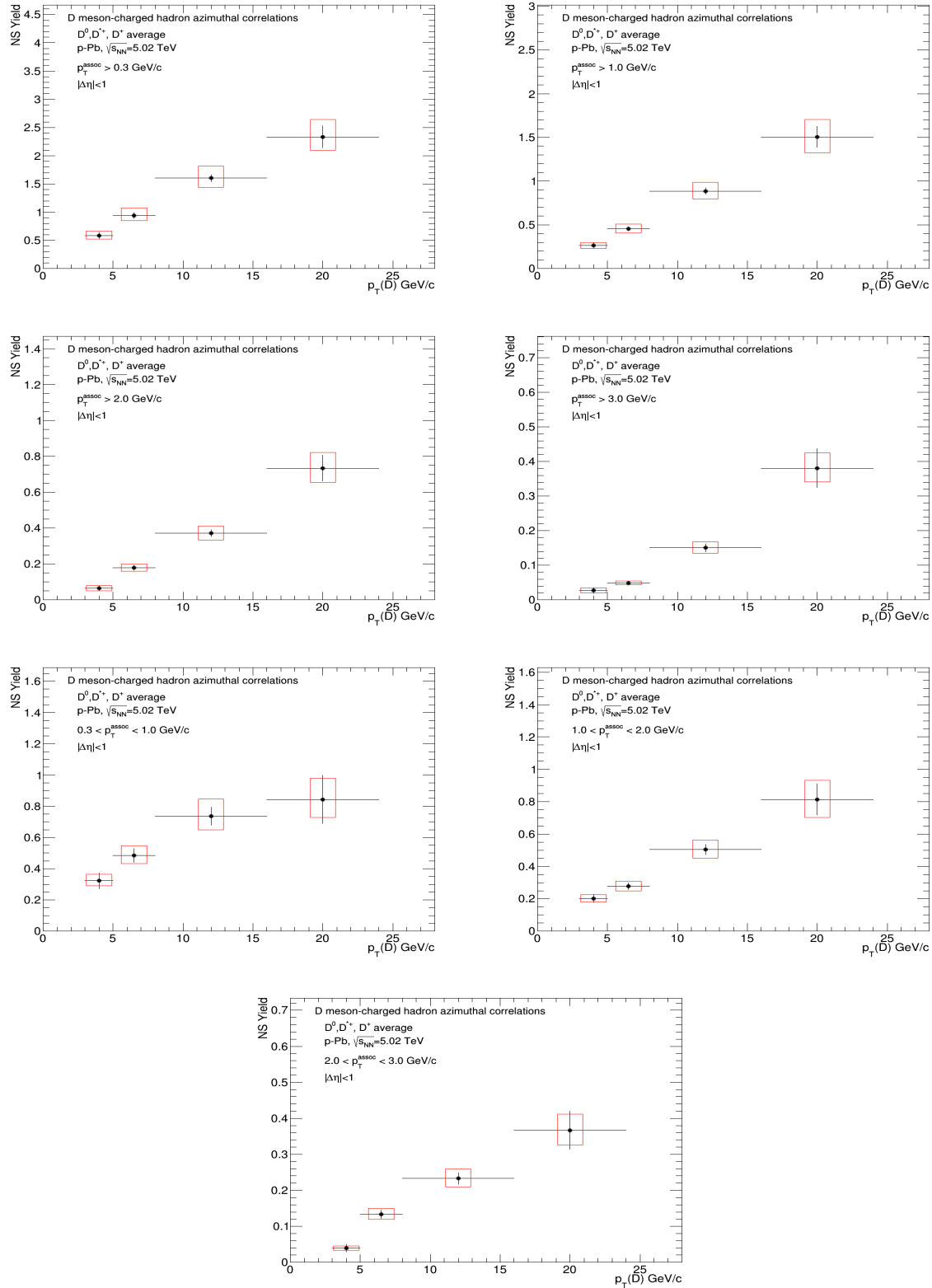
430 follows:

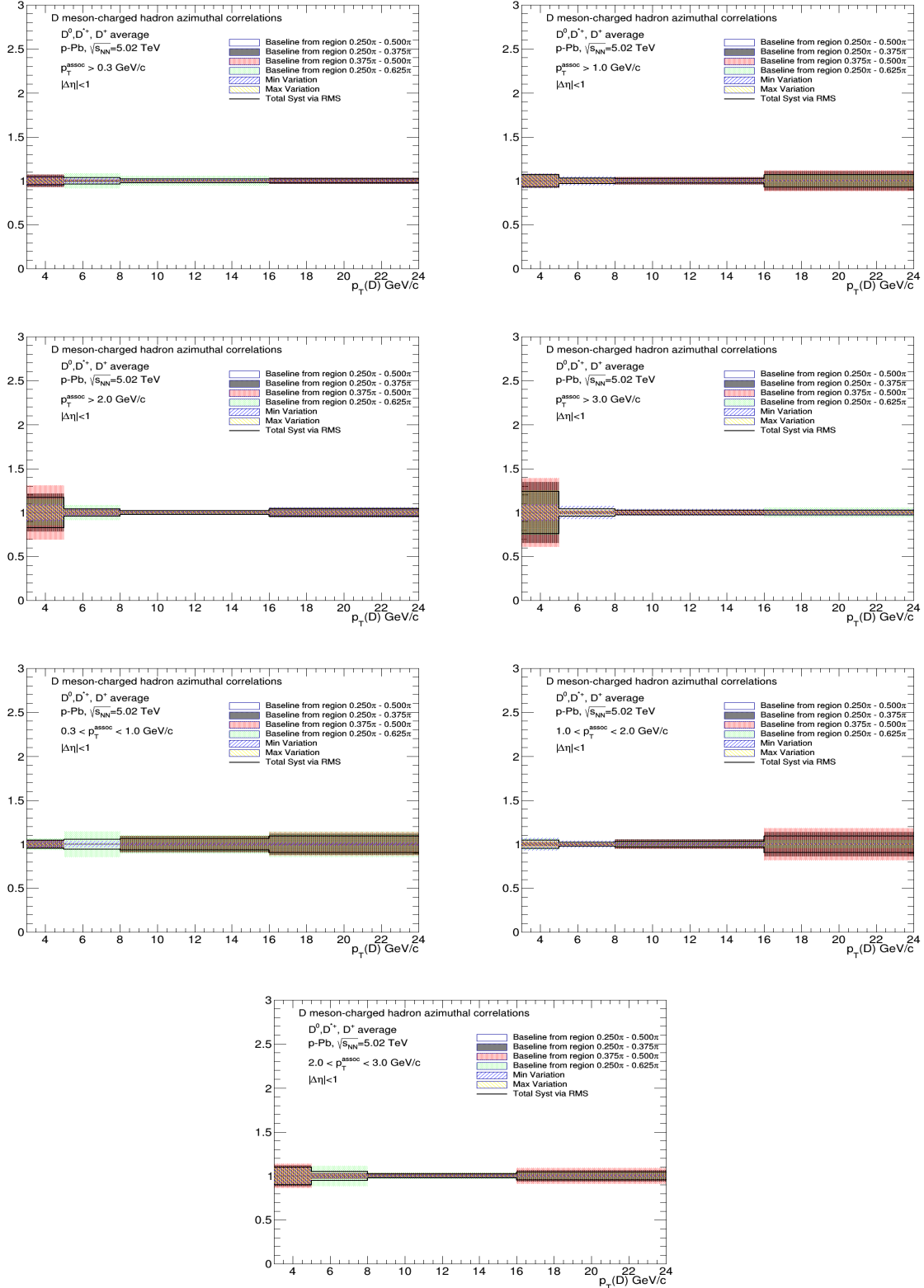
- 431 – The fits are repeated by changing the range of the trasverse region in which the baseline is evaluated. Alternate definitions of  $\frac{\pi}{4} < |\Delta\phi| < \frac{3\pi}{8}$ ,  $\frac{3\pi}{8} < |\Delta\phi| < \frac{\pi}{2}$  and  $\frac{\pi}{4} < |\Delta\phi| < \frac{5\pi}{8}$  are considered.
- 432
- 433 – In addition,  $\Delta\phi$  correlation points are shifted to the upped and lower bounds of their uncorrelated systematic boxes, and the refitted.
- 434
- 435 – The maximum variation of the parameters between the fit outcomes defined in the previous points is considered as systematic uncertainty for the near-side and away-side widths.
- 436
- 437 – For the estimation of the baseline and of the near-side and away-side yields, the previous value is added in quadrature with the  $\Delta\phi$ -correlated systematics in the correlation distributions, since these values are affected by a change in the global normalization of the distributions.
- 438
- 439

$$\sigma^{\text{syst}} = \sqrt{(\text{Max}(\Delta\text{par}^{\text{ped.mode}}, \Delta\text{par}^{\Delta\phi\text{point}}))^2 + (\sigma_{\text{Syst}}^{\text{corr}})^2} \quad (9)$$

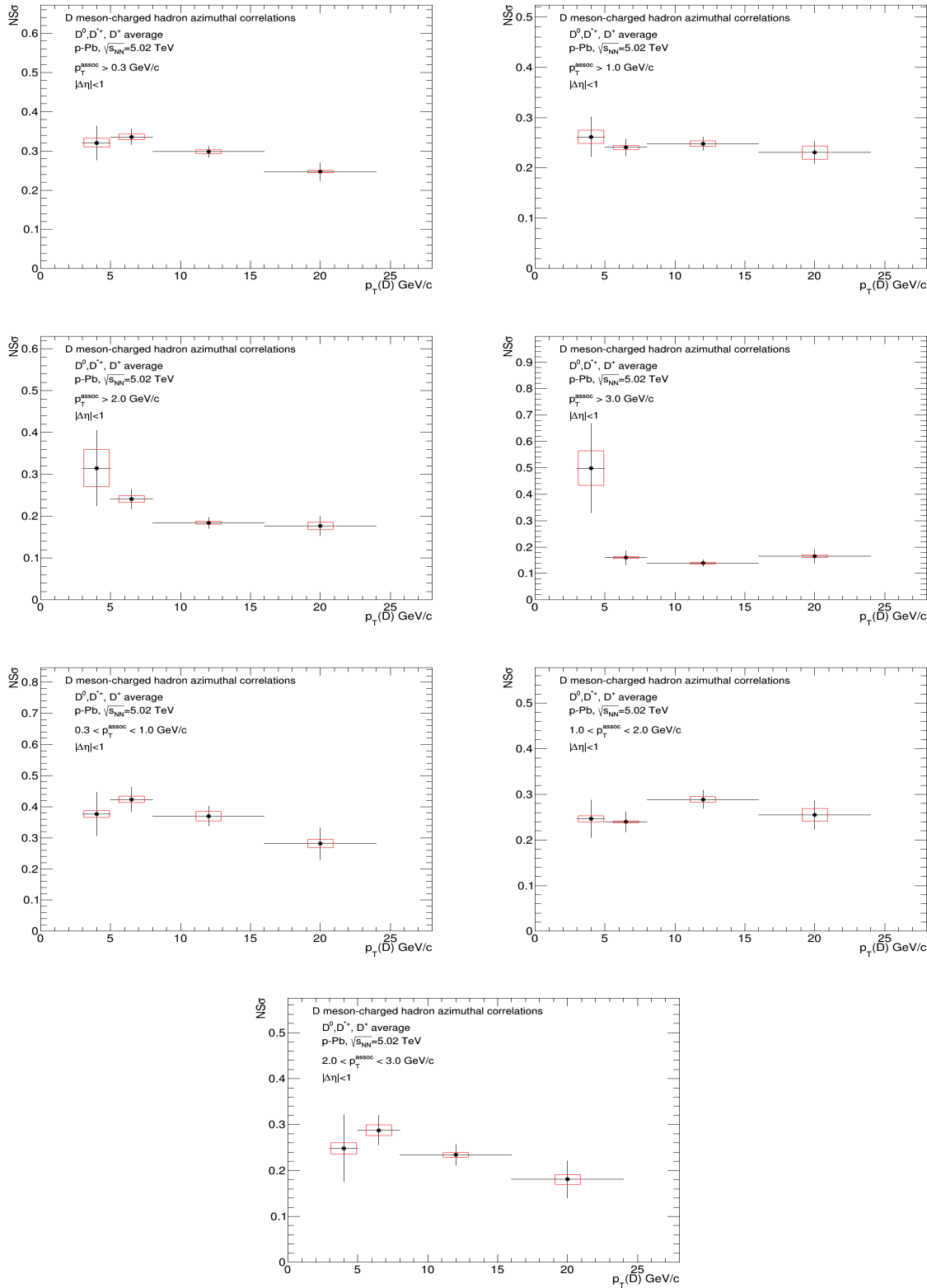
#### 440 5.3.1 Results for near-side yield and width, away-side yield and width, and baseline

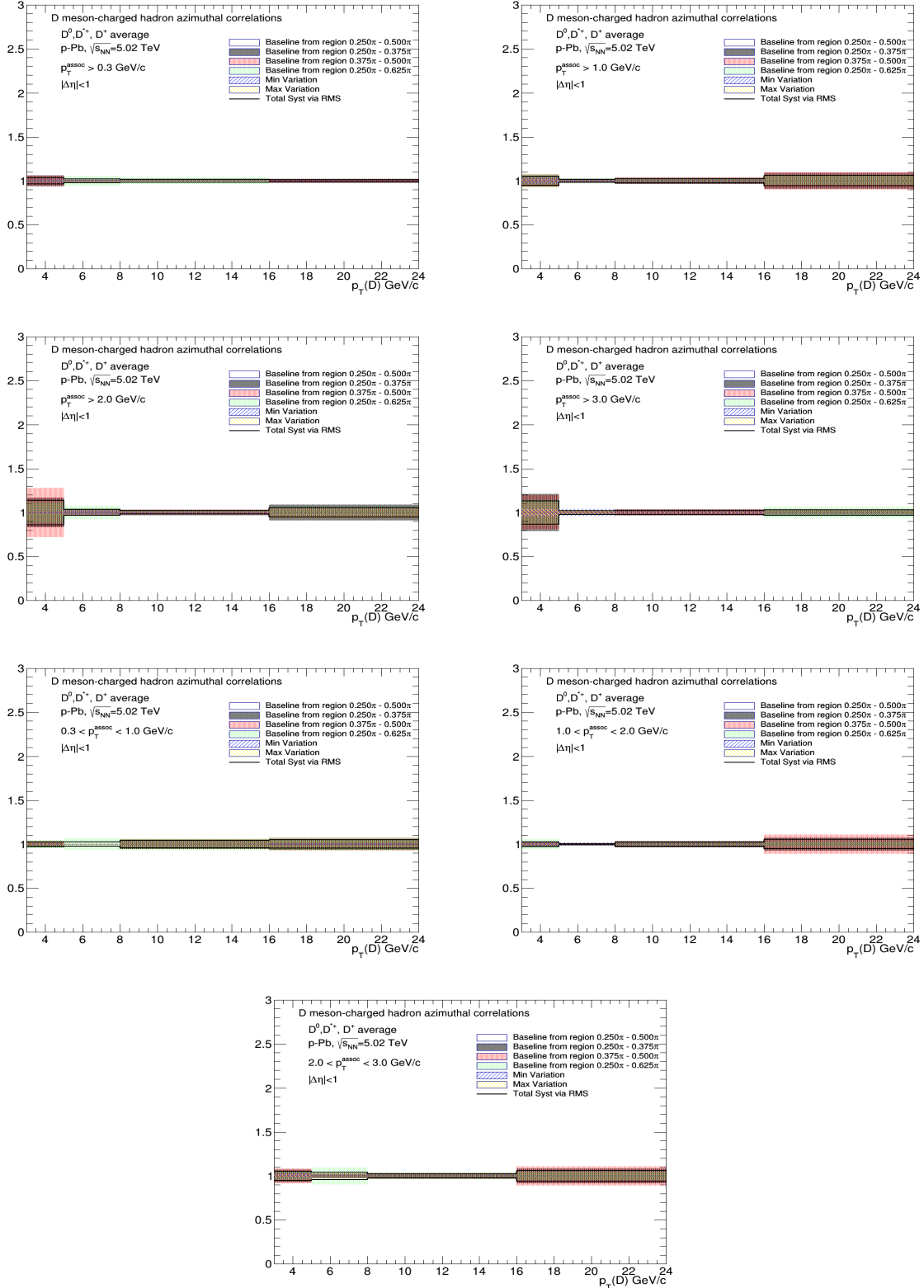
441 Figures 26, 27, 28, 29 and 30 shows the near-side associated yield, width (the sigma of the Gaussian  
 442 part of the fit functions), away-side associated yield, width and the height of the baseline, for the average  
 443 correlation distributions, in the kinematic ranges studied in the analysis, together with their statistical  
 444 and systematic uncertainties **NOTE: the systematic uncertainties are still not fully evaluated, and**  
 445 **will change in the next note version..** For each kinematic range, the correspondent plot showing the  
 446 systematic uncertainty of the considered observable from the variation of the fit procedure is reported  
 447 as well (which is the full systematic uncertainty for the widths). Figures 31, 32, and 33 show the full  
 448 systematic uncertainties for near side yield, away side yield and baseline, with the breakdown of fit  
 449 variation and  $\Delta\phi$  correlated systematic uncertainties. **NOTE: the deltaphi correlated uncertainties**  
 450 **(green boxes) are still not fully evaluated, and will change in the next note version.**



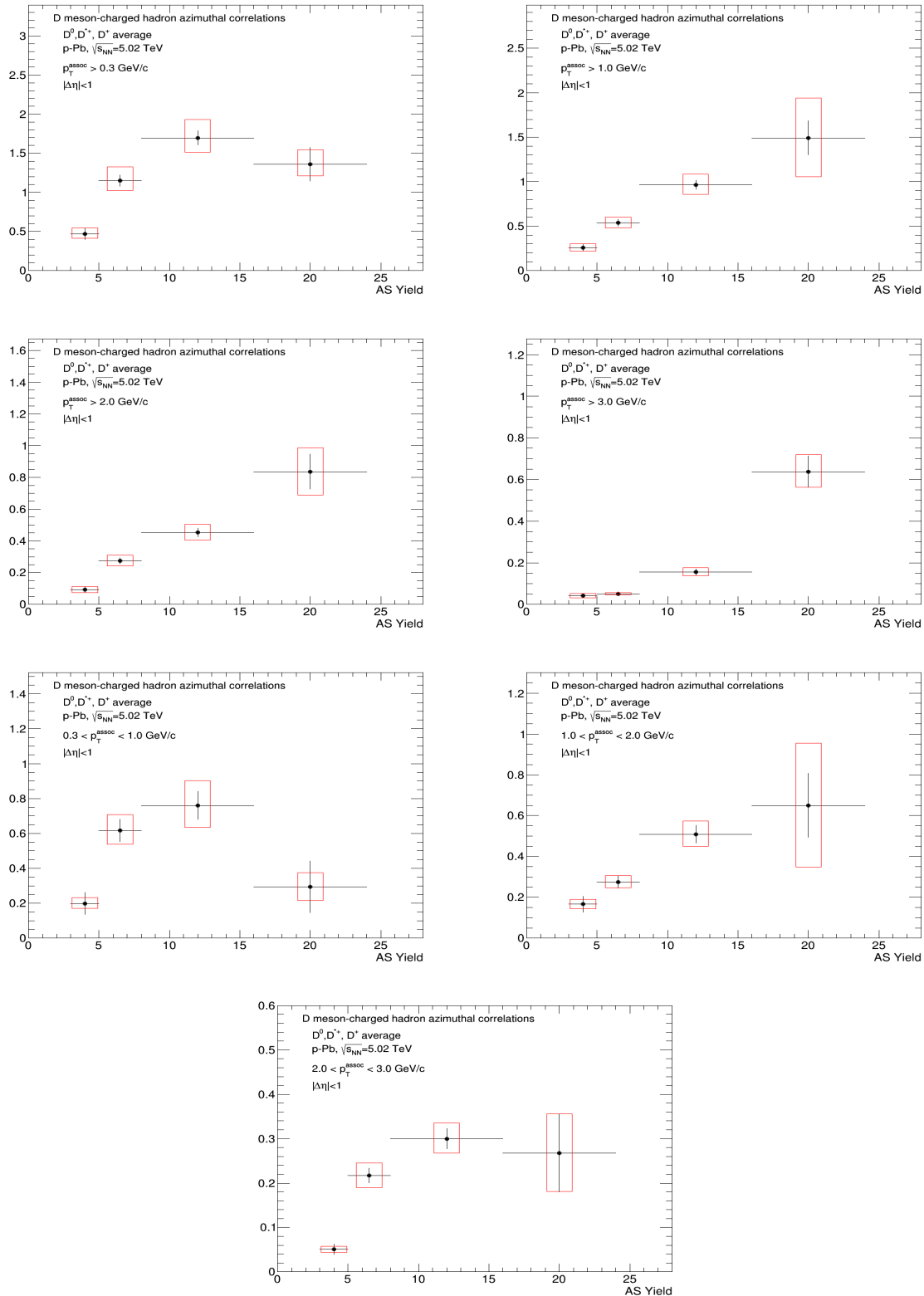


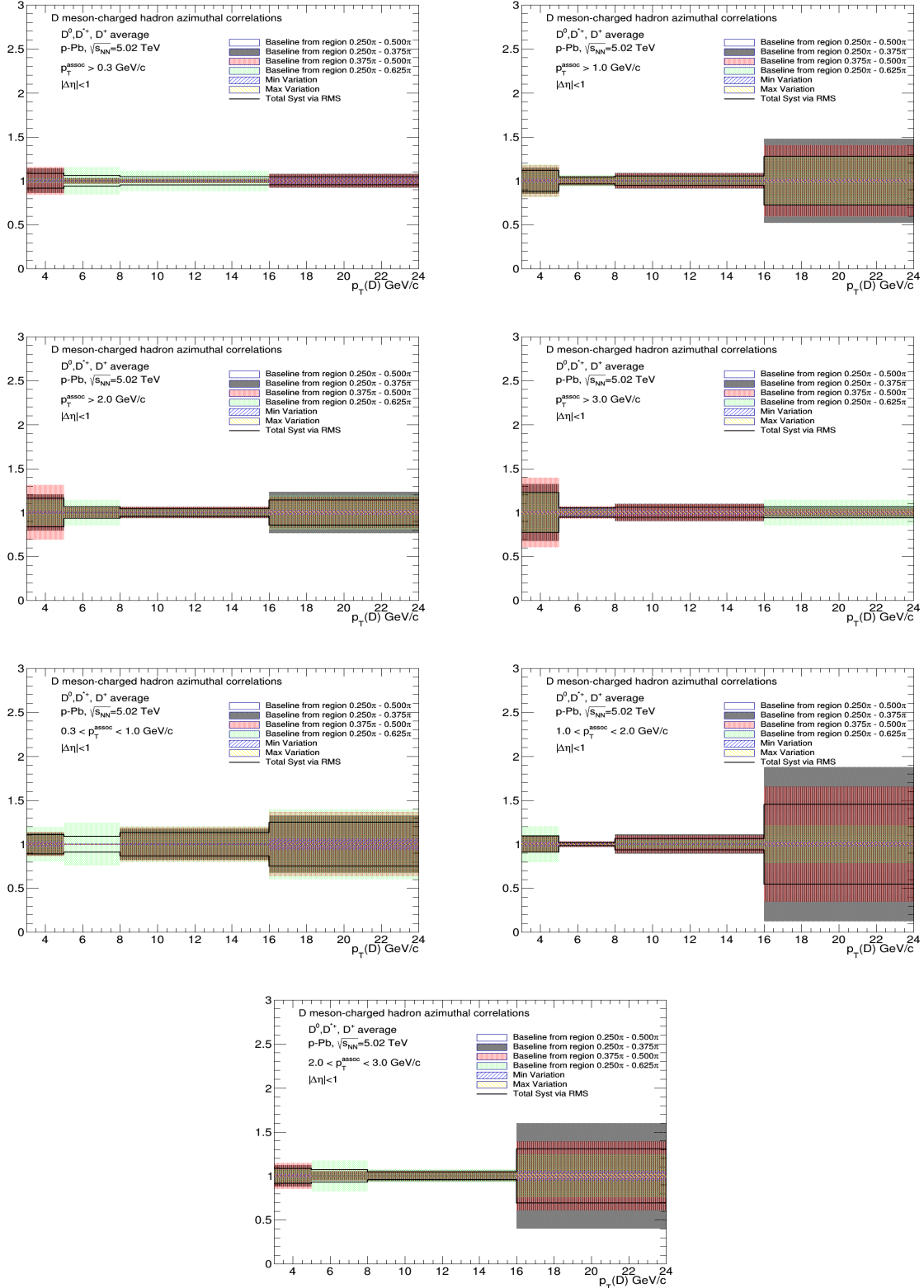
**Figure 26:** Top panels: near side yield  $p_T(D)$  trend for the D-meson average, extracted from fit to the azimuthal correlation distributions, for all the analyzed kinematic ranges of associated track  $p_T$ . Bottom panels: for each kinematic region the systematic uncertainties coming from the variation of the fit procedure are shown.



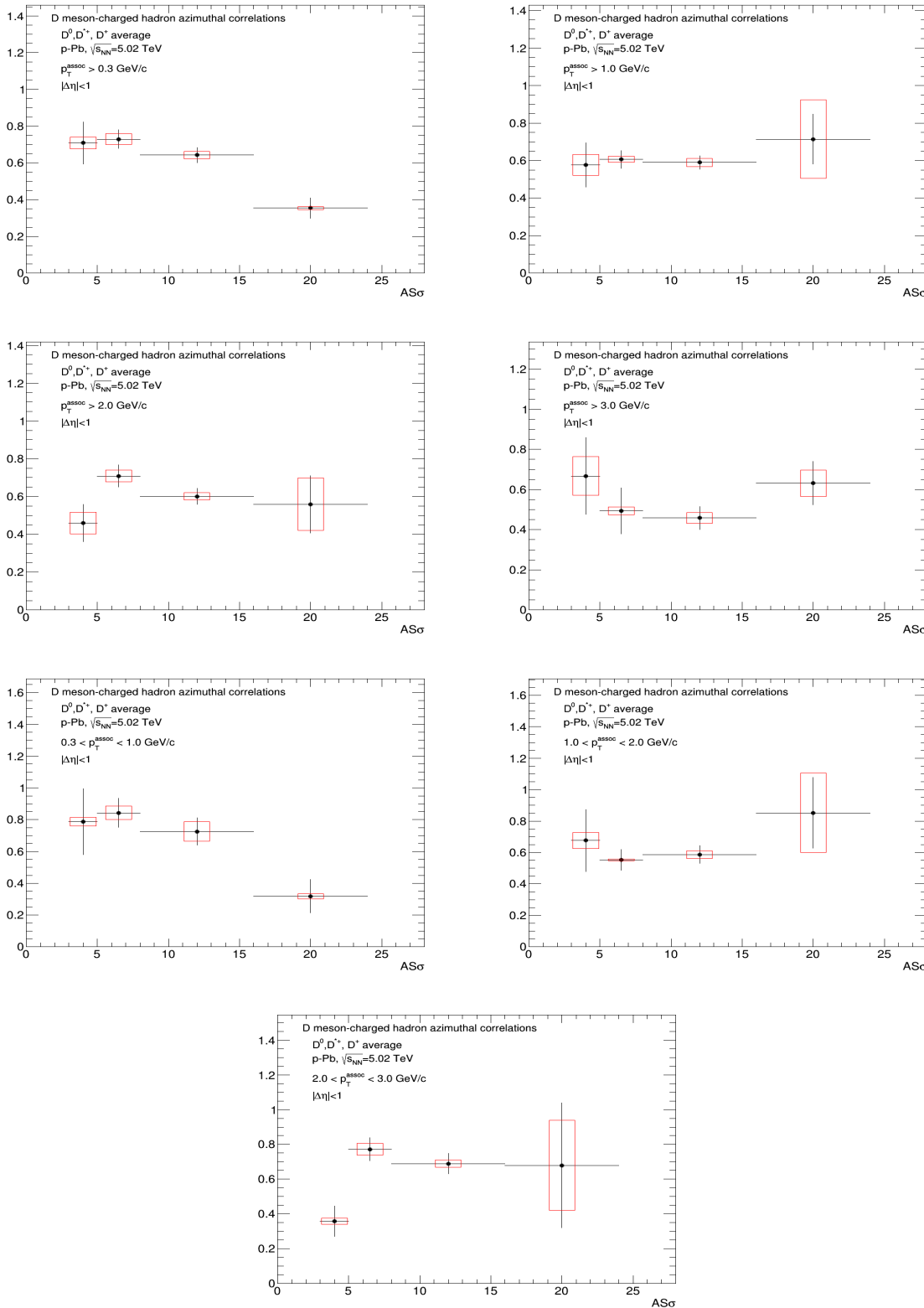


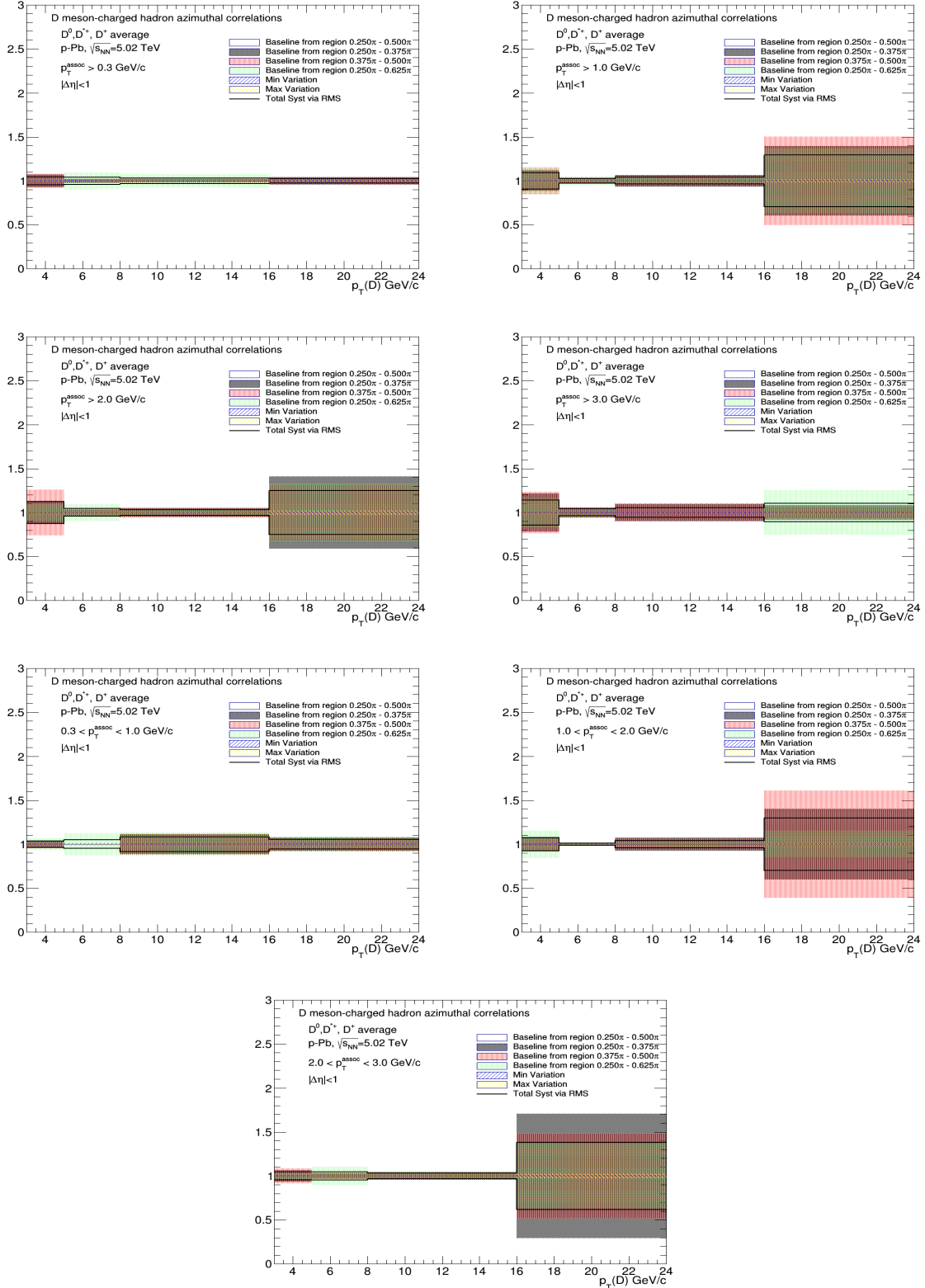
**Figure 27:** Top panels: near side width  $p_T(D)$  trend for the D-meson average, extracted from fit to the azimuthal correlation distributions, for all the analyzed kinematic ranges of associated track  $p_T$ . Bottom panels: for each kinematic region the systematic uncertainties coming from the variation of the fit procedure are shown.



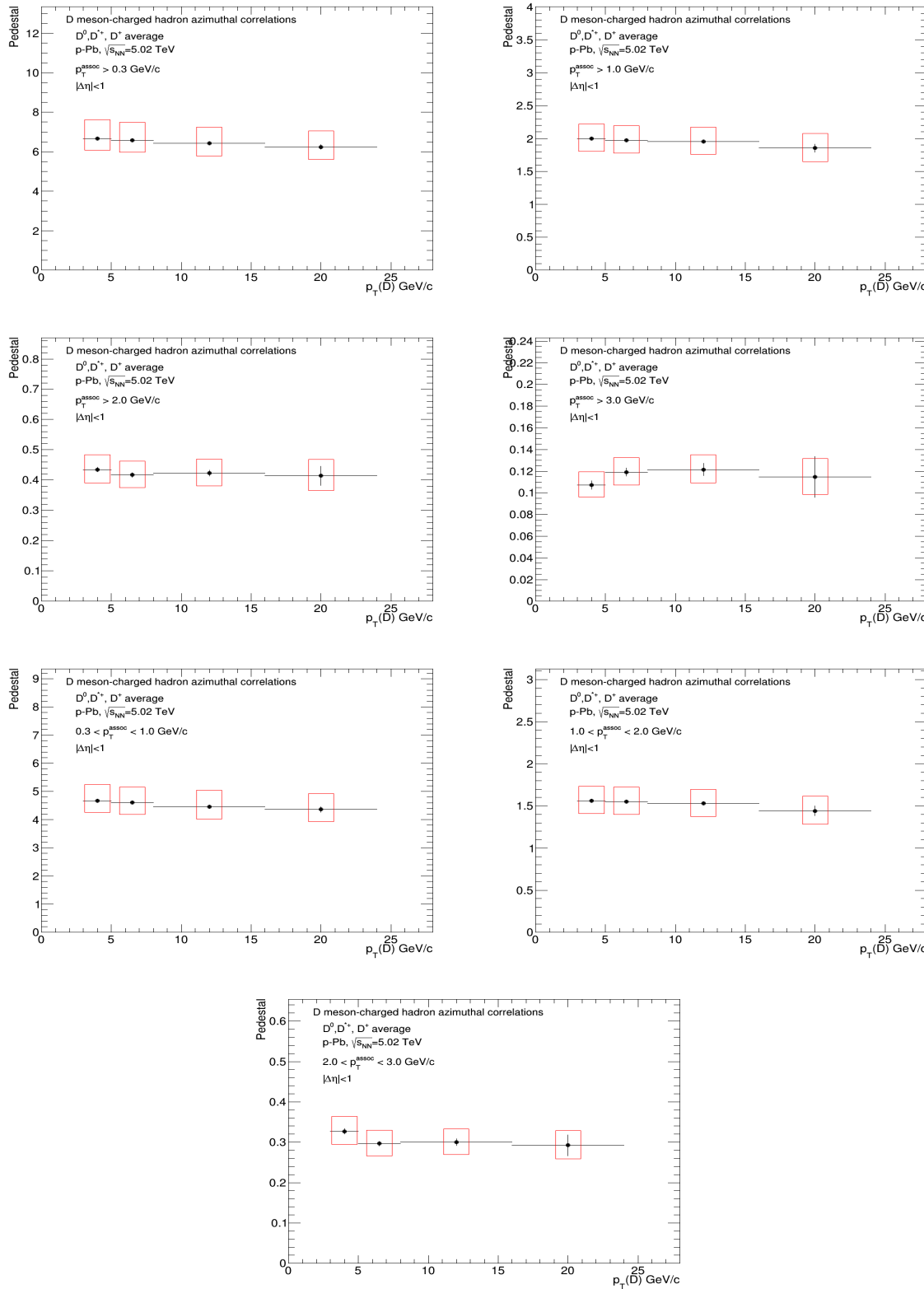


**Figure 28:** Top panels: away side yield  $p_T(D)$  trend for the D-meson average, extracted from fit to the azimuthal correlation distributions, for all the analyzed kinematic ranges of associated track  $p_T$ . Bottom panels: for each kinematic region the systematic uncertainties coming from the variation of the fit procedure are shown.





**Figure 29:** Top panels: away side width  $p_T(D)$  trend for the D-meson average, extracted from fit to the azimuthal correlation distributions, for all the analyzed kinematic ranges of associated track  $p_T$ . Bottom panels: for each kinematic region the systematic uncertainties coming from the variation of the fit procedure are shown.



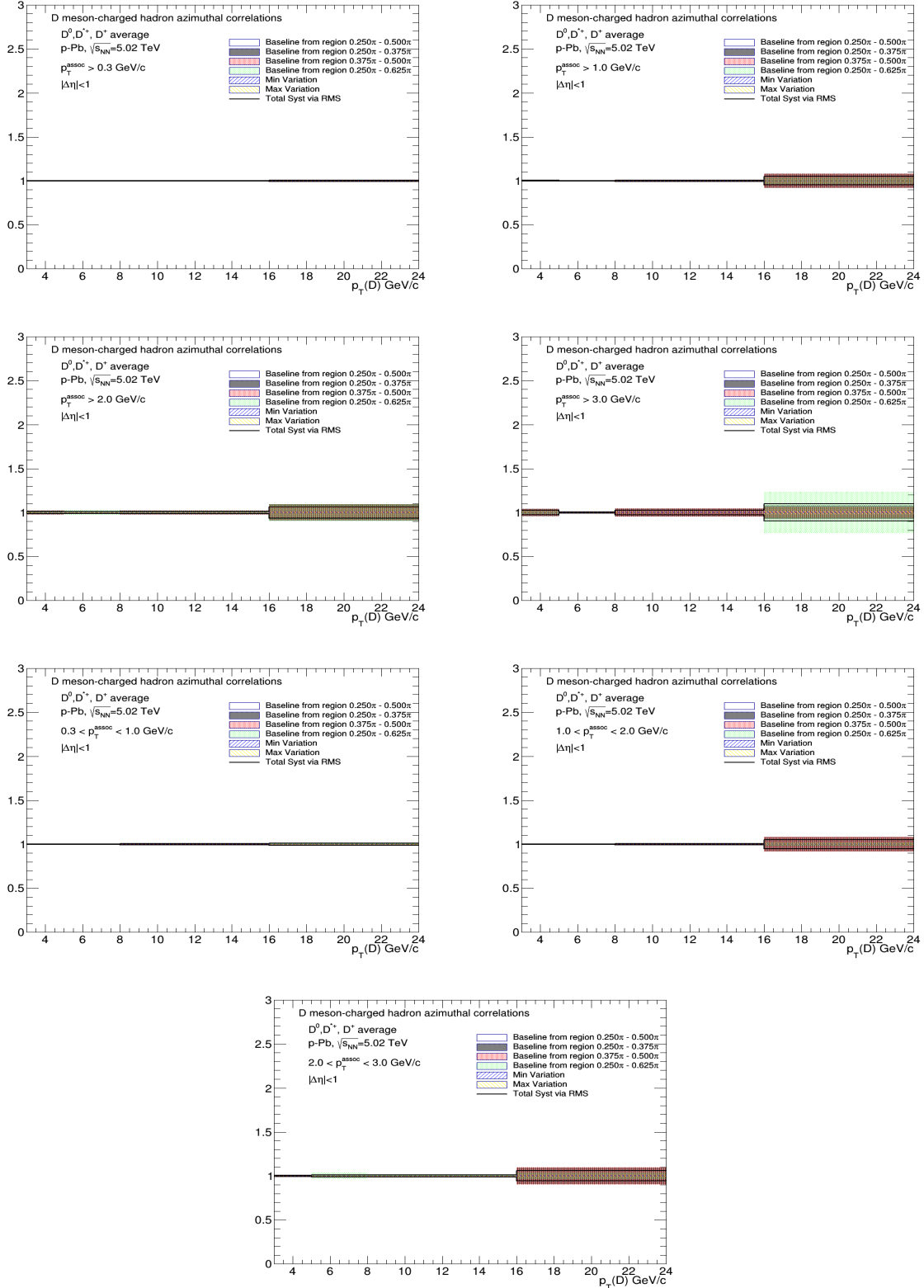


**Figure 30:** Top panels: baseline height trend for the D-meson average, extracted from fit to the azimuthal correlation distributions, for all the analyzed kinematic ranges of associated track  $p_T$ . Bottom panels: for each kinematic region the systematic uncertainties coming from the variation of the fit procedure are shown.

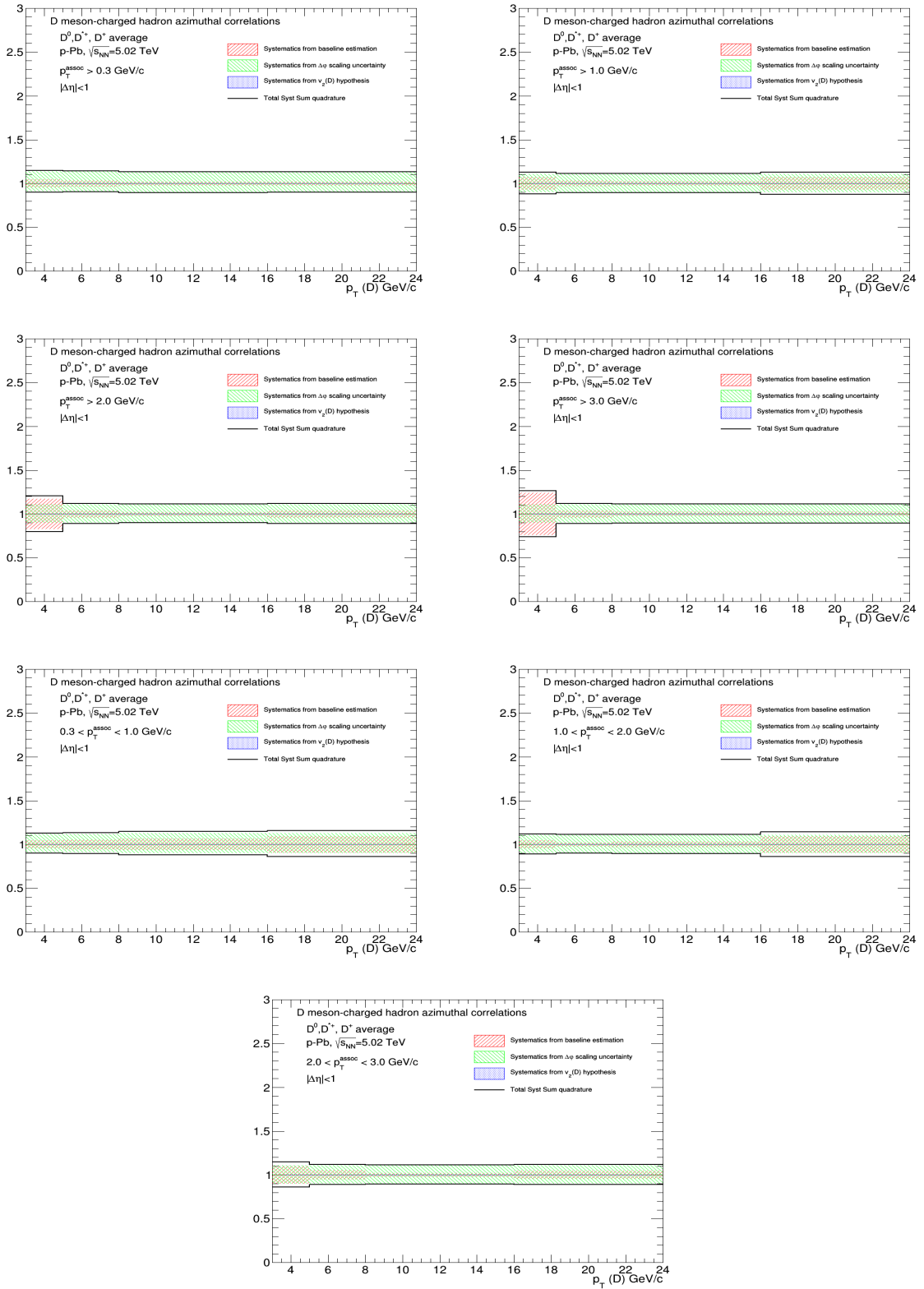


**Figure 31:** Total systematic uncertainty, and its components, for near-side yields in the different kinematic ranges analyzed

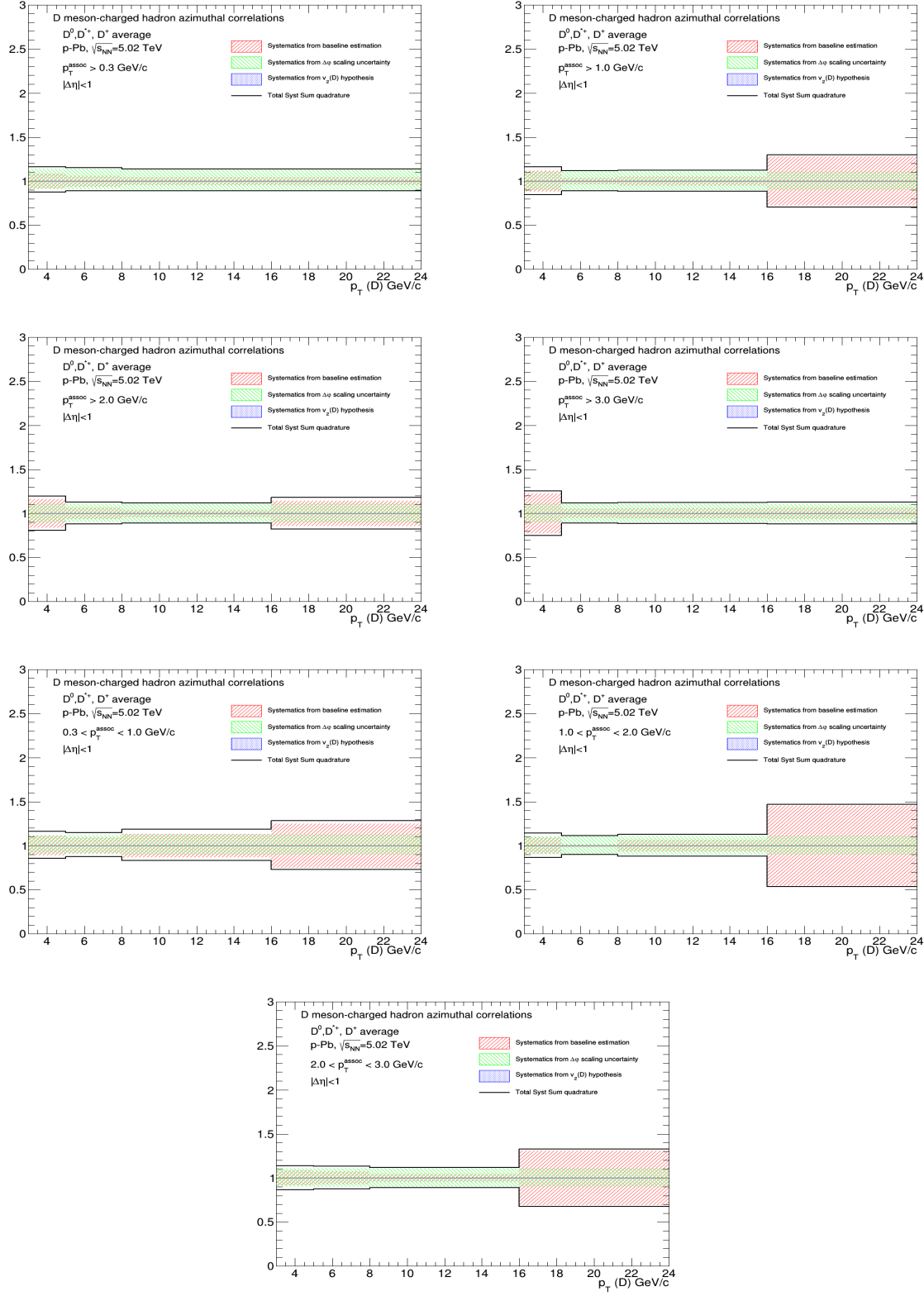


**Figure 32:** Total systematic uncertainty, and its components, for away-side yields in the different kinematic ranges analyzed

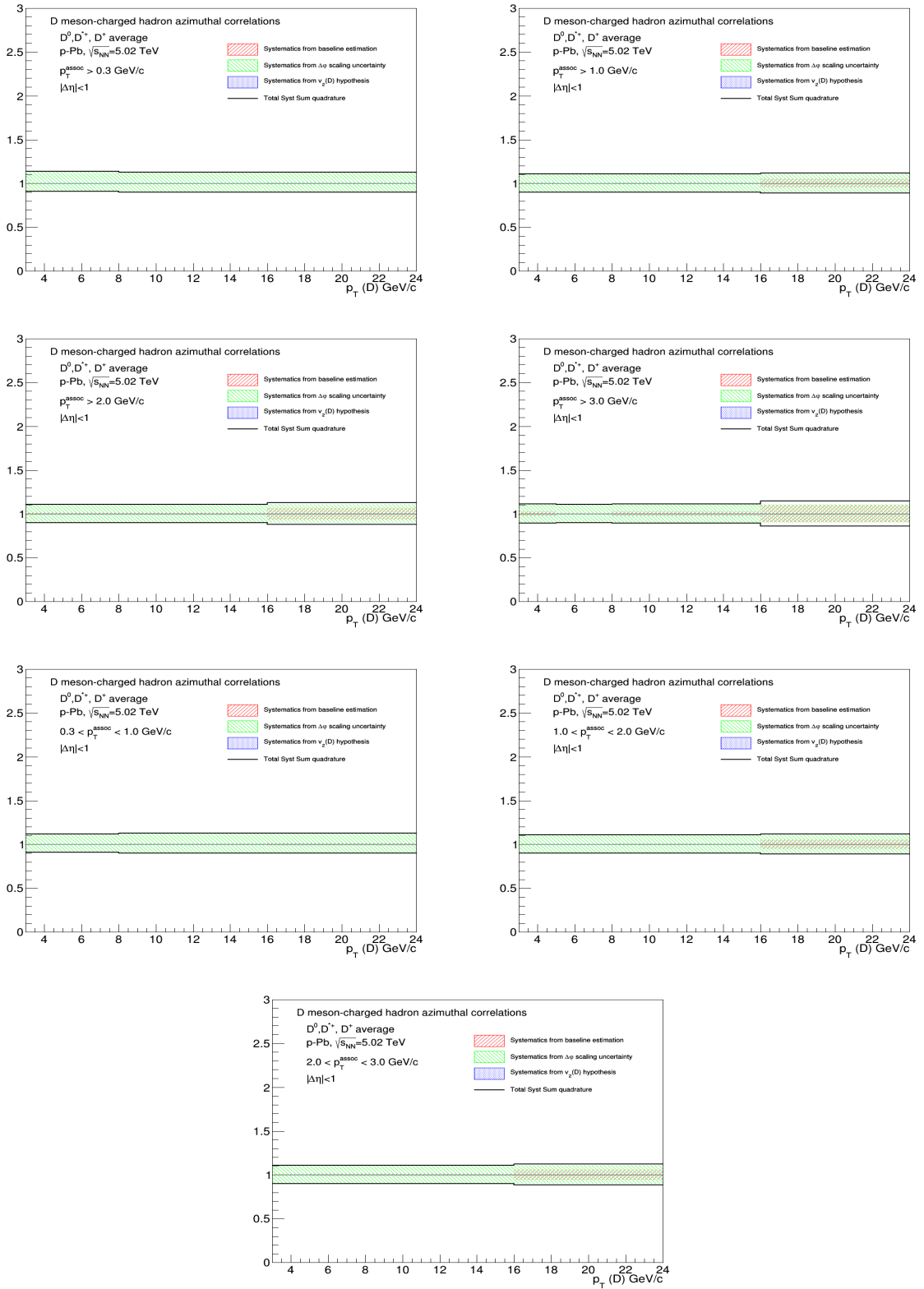


**Figure 33:** Total systematic uncertainty, and its components, for baseline heights in the different kinematic ranges analyzed.

**451 5.4 Planned results for SQM approvals**

452 We are planning to approve the following results (the graphical way of showing the information has still  
453 to be defined):

- 454 – Average D-h correlation distributions, in the different kinematic ranges
- 455 – pT(D),pT(assoc) trend of NS yield, NS width, AS yield, AS sigma, baseline
- 456 – Comparison of correlation distributions with expectations from models (PYTHIA, POWHEG,  
457 EPOS)
- 458 – Comparison of fit observables with expectations from models (PYTHIA, POWHEG, EPOS)
- 459 – (probably) Comparison of correlation distributions and/or fit observables with pp 2010 (and/or pPb  
460 2013) results

<sup>461</sup> **6 Bibliography**

<sup>462</sup> **References**

- <sup>463</sup> [1] B. Abelev et al. [ALICE Collaboration], JHEP **01** (2012) 128.  
<sup>464</sup> [2] B. Abelev et al. [ALICE Collaboration], Eur. Phys. J. C (2017) 77:245.